machines

MDPI

Article

A Digital Twin Model for UAV Control to Lift Irregular-Shaped Payloads Using Robust Model Predictive Control

Umar Farid [1], Bilal Khan [2,3], Sahibzada Muhammad Ali [1] and Zahid Ullah [4,*]

[1] Department of Electrical Engineering, COMSATS University Islamabad, Abbottabad Campus, Abbottabad 22060, Pakistan; umarfarid@cuiatd.edu.pk (U.F.)
[2] Department of Control and Instrumentation Engineering, King Fahd University of Petroleum and Minerals (KFPUM), Dhahran 31261, Saudi Arabia; bilal.khan@kfupm.edu.sa
[3] Center for Sustainable Energy Systems (IRC-SES), King Fahd University of Petroleum and Minerals (KFPUM), Dhahran 31261, Saudi Arabia
[4] Dipartimento di Elettronica, Informazione e Bioingegneria, Politecnio di Milano, 20133 Milano, Italy
* Correspondence: zahid.ullah@polimi.it

Abstract

This paper presents an innovative digital twin (DT) model integrated with robust model predictive control (MPC) to enhance the performance of an unmanned air vehicle (UAV) tasked with lifting and transporting irregular-shaped payloads. Traditional UAV control systems face complex challenges in stability and accuracy when dealing with asymmetrical payloads, as such payloads cause continuous shifts in the center of gravity (CoG) and variable inertial forces, which lead to unpredictable flight dynamics. The proposed DT framework enables the creation of a real-time replica of the UAV payload system. It creates an adaptive control environment that anticipates and mitigates disturbances before they impact the stability of the UAV during a mission. By combining a DT with MPC, the control system dynamically adjusts to variations in payload characteristics, namely (a) changes in mass distribution and (b) aerodynamic drag force. As a result, a stable flight path is ensured even under challenging environmental conditions. The DT model continuously forecasts potential destabilizing events and modifies MPC constraints to accommodate complex shifting dynamics, achieving improved control accuracy and energy efficiency. Extensive simulations across various hanging payload configurations and environmental disturbance scenarios validate the effectiveness of the proposed model. The simulation results show that the DT-MPC strategy significantly improves stability, control precision, and energy conservation, outperforming conventional methods. A comparative analysis is also carried out with a conventional control scheme to validate the robustness of the proposed framework. This research work advances the development of intelligent, autonomous UAV systems capable of reliably managing complex and irregularly shaped payloads with varying mass distributions in real-world scenarios, thereby broadening their potential applications in logistics, emergency response, and industrial transportation.

Keywords: digital twin; model predictive control; UAV stability; irregular payload handling; drone control systems; real-time control; payload dynamics; robust control

check for updates

Academic Editor: Raul D. S. G. Campilho

Received: 13 October 2025
Revised: 7 November 2025
Accepted: 12 November 2025
Published: 20 November 2025

Citation: Farid, U.; Khan, B.; Ali, S.M.; Ullah, Z. A Digital Twin Model for UAV Control to Lift Irregular-Shaped Payloads Using Robust Model Predictive Control. *Machines* **2025**, *13*, 1069. https://doi.org/10.3390/machines13111069

Copyright: © 2025 by the authors. Licensee MDPI, Basel, Switzerland. This article is an open access article distributed under the terms and conditions of the Creative Commons Attribution (CC BY) license (https://creativecommons.org/licenses/by/4.0/).

1. Introduction

UAVs, commonly known as drones, have shown exponential growth in adoption across different sectors, such as (a) logistics, (b) healthcare, (c) agriculture, (d) construction,

(e) industrial inspections [1]. Their capacity to deal with different scenarios and environmental disturbances and access remote locations that are difficult to reach by conventional transport contribute to their indispensability for critical tasks, including package delivery, medical supply transport, crop health surveillance, infrastructure assessment, and search and rescue operations [2]. Their adaptability is important to their lightweight construction, exceptional maneuverability, and cost-effective operations [3]. Although UAVs are widely used for payload transportation duties, they face irregular loads characterized by asymmetric shapes, uneven mass distributions, and interconnected aerodynamic profiles [4].

The hanging of irregular payloads poses a significant issue to the stability, security, and control performance of UAVs [5]. Non-uniform loads can be dynamic during flight and will perturb the CoG and rotational inertia of the UAV. They affect equilibrium because UAVs are unable to track reference trajectories and orientations [6]. However, these inconsistent payloads have asymmetrical geometry and exhibit different aerodynamic forces depending on altitude, forward motion, and velocity [7]. These multiple disturbances eventually lead to flight operation instabilities in UAVs, contributing to the reasoning behind control paradigms [5].

With autonomous UAV operations, which cannot be managed manually, stability and safety requirements are necessary [8]. Complex control systems are mandatory to maintain stability and accuracy in the presence of perturbations [9]. Reducing irregular payload-related control hurdles has garnered significant attention from both academics and industry [10]. In such situations, an increase in UAV autonomy opens the door to revolutionary possibilities in logistics, disaster relief, and industrial logistics, where valuable heterogeneous loads can be smoothly managed with insignificant chances of failure [11].

Asymmetric payload delivery presents unique control complexities in UAVs, as these payloads are very unlike symmetric and predictable cargoes [12]. Doubts in exact mass and aerodynamic characteristics initiate continuous CoG disturbance, varying inertial moments, and arbitrary drag/lift distributions, making stable flight challenging [13]. As an example, regarding long or asymmetrical delivery, payload motions or transfers can be excited because of agile maneuvers, causing UAV destabilization [14].

Traditional controllers such as PID or MPC assume constant or predictable payload characteristics [15]. These principles fail with non-regular payloads, whose characteristics are adaptive to UAV kinematics and non-cooperation [16]. Conventional systems exhibit sluggish responses, require reconfiguration to load variances, and display reactive disturbance responses, which increase instability, precision issues, and energy consumption in control efforts [17].

The need to have real-time dynamic paradigms to maneuver through irregular payload transportation is important, as they enhance autonomous transfer without disturbing stability, efficiency, or security [18]. A DT is a type of virtual system that replicates the kinetics of a physical entity in real time [19]. The DT predicts interruptions, which is enabled by copying the UAV–payload interactions, enabling predictive control [20]. The DT utilizes information collected by UAV sensors, which enables it to maintain a correct virtual representation of the UAV, forecast future alterations, and detect itself just before future disturbances will impact the system [21].

Integrating a DT and MPC provides the UAV controller with a system that can overcome anomalies in the payload [21]. Robust MPC is good in stochastic prediction as it uses uncertainties in optimization [22]. It can support reallocation of payload mass, aerodynamic perturbation, and migration of CoG, enhancing disturbance resilience [23]. DT-supplied foresight allows unrelenting control input refinements, compensating payload perturbations during flight operation and maintaining stability at the expense of energetics [24].

This integration not only solves the problem of irregular payload management, but it brings improvements in efficiency and safety of transportation using UAVs [25].

2. Related Work

This section reviews prior research across three key areas relevant to this study: (1) DT technology in autonomous systems, particularly UAVs; (2) MPC for UAV stability; (3) control strategies for managing irregularly shaped payloads. Collectively, these works outline the current state of the art, highlighting gaps in the control of UAVs with complex payloads.

2.1. Digital Twin Technology in Autonomous Systems

DT technology has become a transformational methodology in manufacturing and autonomous systems, enabling the generation of real-time virtual copies of physical systems [26]. DTs facilitate real-time monitoring, diagnostics, and control by enabling data-driven simulations and predictions [27]. Investigations have developed the principles of DTs and their flexibility in working under dynamic environments, which is essential for making real-time decisions [28]. Within the framework of autonomous UAVs, DTs are used frequently to simulate the real-world situation virtually [29]. Recent papers have investigated the potential of DTs in decision-making in aerospace markets, showing greater reliability in hard operations. Predicting faults with the help of DTs enhances the safety and efficiency of UAVs [30], and enhanced models facilitate the simulation of the complex dynamics of UAVs and enable the implementation of intricate corrections.

DT applications have been developed on resilient swarms of UAVs, involving edge computing to provide low-latency synchronization [31]. Physical models with machine learning Hybrid DTs are better for predictive maintenance in unpredictable environments [32]. Federated DTs support collaborative work of multiple agents without information exchange, which is needed for use with privacy-sensitive UAV flocks [33]. Moreover, irregular payloads are still limited in DT applications, necessitating dynamic models that capture variable loading conditions [34]. This paper develops the DT-UAV combination by combining it with robust MPC to estimate and avoid destabilizing factors and extrapolate DT utility to complex tasks [21].

2.2. Model Predictive Control for UAV Stabilization

MPC is also actively applied in UAVs to deal with multi-variable constraints when operating in dynamic environments [35]. Contrary to conventional approaches, MPC forecasts the behavior of a system with a receding horizon, predicting disturbances and responding to changes in paths, which are essential for UAV stability, as presented in [36]. Principles of MPC have been elaborated through theoretic frameworks, where the benefits and shortcomings of linear and nonlinear models have been noted. Optimization of UAV reference trajectories in varying environments demonstrates the efficiency of MPC, and UAV stability results are studied in relation to the influence of disturbances, with restricted ability to model variable payloads [37].

The latest developments include stochastic MPC, which addresses uncertainties and optimum loading due to payload variations, and adaptive MPC, which handles irregularly changing slung loads [38]. The authors of [39] present innovations in learning-enhanced MPC for online parameter tuning in turbulent conditions. The authors of [40] present innovations in distributed MPC for UAV formations with payload differences. Reference [41] discusses the topic of event-driven MPC to reduce computational load in resource-constrained UAVs. MPC is resilient because it counters disturbances at a high level [23]. This study integrates DTs and MPC, where the real-time feedback of a DT enables adaptation to irregular dynamics, thereby enhancing stability and precision [21].

2.3. Control Strategies for Irregularly Shaped Payloads

The problem of irregular payloads is caused by their generated oscillations, changes in the CoG, and aerodynamic influence [42]. Conventional UAV control requires symmetry; hence, it is not suitable when there are such irregularities. The literature on suspended-load steadiness has highlighted destabilizing forces in a manner similar to CoG-variant irregularities [43]. Adaptive nonlinear control techniques have been employed to address problems with varying loads, which pose challenges in tuning and limit real-time flexibility [44]. Unknown payload-adaptive hybrids exhibit flexibility, but cannot handle sudden changes [45]. Reduced-order models of irregular payloads can accurately display the effects of a load on trajectory, highlighting the importance of understanding the disturbances that affect stability.

The latest advances are vision-based adaptive controls to dictate payload with no sensors [46], reinforcement learning to navigate nonlinearities with slung irregular loads [47], and sliding-mode observers to neutralize aerodynamic disturbances in asymmetric lifts [48]. The authors of [12] explain the Distributed Sliding-Mode Controller for single and heterogeneous drones used for transportation of a hanging payload. However, real-time dynamic adaptation remains unexplored, as it is not yet supported by kinetic simulations. DTs offer a solution through real-time, data-driven UAV–payload simulations, predicting anomalies for robust control. In this study's DT–robust MPC framework, responses to irregular loads are enhanced with superior stability and precision, addressing adaptive shortcomings in payload variations. In [49], the authors investigate the operation of an aerial manipulator system equipped with a controllable arm with two degrees of freedom to carry out actuation tasks during flight operation. A novel low-altitude vehicle speed detector system utilizing UAVs for remote sensing applications in smart cities is introduced in [50], aiming to enhance traffic safety and security. Similarly, the authors present a novel approach to autonomous payload delivery for single and multiple heterogeneous UAVs in [51]. For single-UAV operations, SMC enables a UAV to track a predefined reference trajectory, autonomously identify the payload's CoM, securely attach to it, lift it, and deliver it to the desired target location.

2.4. Summary and Research Gap

Existing research in the literature confirms the individual strengths of DTs and MPC in UAV control, prediction, and disturbance rejection. DTs provide accurate simulations for identifying and monitoring UAVs. Meanwhile, MPCs manage unstable environments and uncertainties, ensuring the stability of UAVs in harsh conditions.

However, there is a research gap: the integration of DTs with the MPC of hanging irregular-payload delivery is not examined in detail. The literature shows the use of conventional approaches, which lack the capability to forecast the problems of hanging payloads in real time. Furthermore, MPC, useful in response to environmental disturbances in the case of constant conditions, experiences troubles with variable hanging payloads.

The proposed research paper will fill this gap by integrating DTs with MPC to enhance the adaptability and stability of real-time flights by UAVs in terms of irregularly loaded payloads. The predictive features of DTs enable the rejection of disturbances in advance, whereas MPC allows for tighter control using forecasts, which is necessary for stability in the face of load variations. This method ensures flexible, accurate, and effective solutions for UAVs with hanging payloads, thereby widening reliability in various applications. It also leads the way in autonomous operations in complex and demanding environments by applying the use of DT predictions and MPC to achieve safer and cost-efficient transportation of irregular payloads.

The key contributions of the paper to the aforementioned research gaps are as follows:

- **Real-Time DT of Irregular Payload Kinetics:** In this paper, the authors present a DT framework for a UAV carrying an irregularly shaped hanging payload, which extends the current DT models beyond operation only in the case of a static environment. The DT dynamically recreates time-varying payload properties, including mass reallocation, CoG variations, and aerodynamic behavior, which gives a digital platform for predictive control and mitigation of disturbances.
- **DT-MPC Integration:** The present work combines the DT and MPC, making possible the adaptive and precise control of UAVs even in the case of complicated payloads. This hybrid command utilizes real-time data from a DT to support MPC in managing uncertainties, ensuring stability and efficiency when other classic control methods fail.
- **Adaptive Predictive Disturbance Mitigation:** We propose a new adaptive predictive rejection mechanism with the use of DT measurements of payload-induced disturbance. This gives MPC the opportunity to make early corrections to control inputs, minimize oscillations, maximize energy consumption, and enhance stability during flight with highly variable payload geometries throughout the mission.
- **Validation Across Diverse Payloads:** The study validates the DT-MPC framework through extensive simulations across a wide range of payload configurations, addressing real-world irregularities. The results indicate that DT-MPC yields better performance in terms of stability, precision, and energy efficiency, establishing a robust foundation for autonomous UAV operations with irregular hanging payloads.

Table 1 compares the contribution of this paper with state-of-the-art literature work.

Table 1. Comparison of Contributions with State-of-the-Art.

Contribution	Novelty vs. Prior Art
1. Real-Time DT for Irregular Payload Kinetics	Unlike [36], we model time-varying $m_p(t)$, $r_p(t)$, and $I_p(t)$ using online identification.
2. DT–Robust MPC Synergy	We are the first to use DT forecasts to update MPC & tube bounds in real time (Section 3.3.3).
3. Adaptive Predictive Disturbance Mitigation	We achieve pre-emptive control via ARIMA-disturbance forecasting, not reactive control like in [51].
4. Comprehensive Validation	We present 18 figures across diverse irregular payloads + disturbances, beyond [46].

The rest of the paper consists of Section 3, explaining the modeling and architecture in detail; Section 4, explaining the problem formulation and analysis: Section 5, which presents detailed simulation results to validate the proposed work; and Section 6, which concludes the paper and gives some future directions.

3. System Architecture

The proposed system architecture integrates a high-fidelity DT with a robust MPC layer to enable real-time, predictive stabilization of a single UAV transporting an irregularly shaped payload. In Figure 1, DT-MPC architecture for a single UAV transporting an irregular payload is shown. Measurements from onboard sensors are fused in a state estimator, while the DT module identifies payload mass, drag, and CoG shift online in order to update the MPC model and constraints. Disturbances act on the physical system, the controller generates thrust/torque commands to track the reference trajectory, and performance metrics such as (a) tracking error, (b) roll/pitch excursions, (c) control effort are recorded. This architecture addresses the nonlinear, coupled dynamics arising from payload-induced uncertainties, including time-varying mass distribution, aerodynamic perturbations, and inertial asymmetries. The framework is hierarchically designed, com-

prising the following elements: (i) the UAV–payload dynamics framework, which is a 6-DoF rigid-body equation, with the addition of the payload; (ii) the DT framework, which offers high-resolution predictive simulations based on the augmentation of the state and the use of Kalman filtering; (iii) the robust MPC layer, which optimizes the control inputs within the framework of uncertainty bounds and stability constraints. Rigorous mathematical validation ensures asymptotic stability and constraint satisfaction under bounded disturbances.

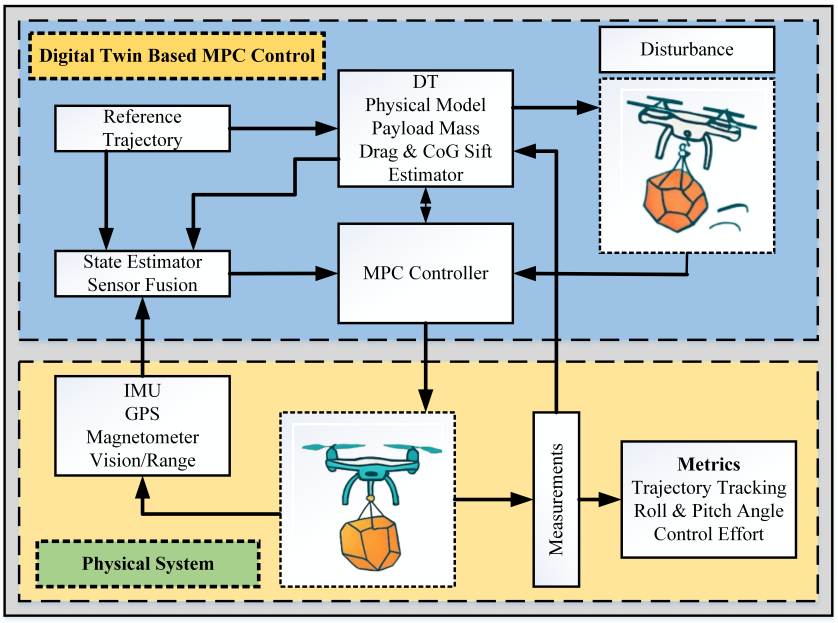


Figure 1. System architecture of Digital Twin Based MPC for payload delivery.

3.1. UAV and Payload Dynamics Model

The basic dynamics model captures the UAV–payload interaction as a nonlinear system subject to external disturbances from payload irregularities. Figure 2 presents the schematic diagram of a UAV with a hanging payload.

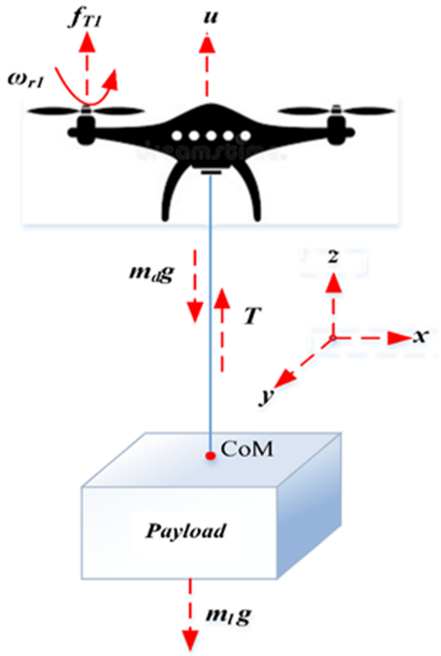


Figure 2. Schematic diagram of UAV with payload.

3.1.1. UAV Flight Dynamics

The UAV's 6-DoF motion is governed by the Newton–Euler equations in the body-fixed frame $\mathcal{B}$, transformed to the inertial frame $\mathcal{I}$ via the rotation matrix $R \in R^3$. Let $p \in R^3$ denote the position in $\mathcal{I}$, $\mathbf{v} \in \mathbb{R}^3$ the velocity in $\mathcal{B}$, $\boldsymbol{\omega} \in \mathbb{R}^3$ the angular velocity in $\mathcal{B}$, $m > 0$ the UAV mass, and $I \in \mathbb{R}^{3\times3}$ the positive definite inertia tensor.

The translational dynamics are

$$m\dot{\mathbf{v}} = R^T(m\mathbf{g} + \mathbf{f}_t + \mathbf{f}_d + \mathbf{f}_p) - m\boldsymbol{\omega} \times \mathbf{v}, \tag{1}$$

where $\mathbf{g} = [0, 0, -g]^T$ is gravity ($g = 9.81\,\mathrm{m/s^2}$), $\mathbf{f}_t = [0, 0, T]^T$ is the collective thrust ($T > 0$), $\mathbf{f}_d = -\frac{1}{2}\rho\|\mathbf{v}\|^2 C_d A \frac{\mathbf{v}}{\|\mathbf{v}\|}$ is drag ($\rho > 0$ air density, $C_d > 0$ drag coefficient, $A > 0$ reference area), and $\mathbf{f}_p$ is the payload force (detailed in Section 3.1.2).

The rotational dynamics are

$$I\dot{\boldsymbol{\omega}} + \boldsymbol{\omega} \times (I\boldsymbol{\omega}) = \boldsymbol{\tau}_t + \boldsymbol{\tau}_p, \tag{2}$$

where $\boldsymbol{\tau}_t = [\tau_x, \tau_y, \tau_z]^T$, attitude torques from differential rotor speeds, and $\boldsymbol{\tau}_p$ is the payload torque.

In state-space form, the nominal UAV dynamics are $\dot{\mathbf{x}} = f(\mathbf{x}, \mathbf{u})$, where $\mathbf{x} = [\mathbf{p}^T, \mathbf{v}^T, \boldsymbol{\theta}^T, \boldsymbol{\omega}^T]^T \in \mathbb{R}^{12}$ ($\boldsymbol{\theta}$ Euler angles) and $\mathbf{u} = [T, \tau_x, \tau_y, \tau_z]^T \in \mathbb{R}^4$.

Theorem 1. *For any equilibrium* $(\mathbf{x}_e, \mathbf{u}_e)$ *where* $\boldsymbol{\omega}_e = \mathbf{0}$ *and* $\mathbf{v}_e = \mathbf{0}$*, the dynamics admit a local linearization* $\dot{\mathbf{z}} = A\mathbf{z} + B\mathbf{w}$*, with* $\mathbf{z} = \mathbf{x} - \mathbf{x}_e$*,* $A = \frac{\partial f}{\partial \mathbf{x}}|_{\mathbf{x}_e}$*,* $B = \frac{\partial f}{\partial \mathbf{u}}|_{\mathbf{u}_e}$*, and* $\mathbf{w}$ *a perturbation input, provided the Coriolis terms are Lipschitz-continuous (bounded by* $L > 0$*).*

Proof. By the inverse function theorem, since f is C^1 and the Jacobian A is Hurwitz for small perturbations (as $I \succ 0$), the linearization holds in a neighborhood $\|\mathbf{z}\| < \delta$. □

3.1.2. Payload Dynamics

The irregular payload introduces time-varying parameters: let $m_p(t) > 0$ be the payload mass, $\mathbf{r}_p(t) \in \mathbb{R}^3$ the relative position vector from the UAV center of mass (CoM), $I_p(t) \in \mathbb{R}^{3\times3}$ the payload inertia tensor, and $\mathbf{v}_p = \dot{\mathbf{r}}_p + \mathbf{v} + \boldsymbol{\omega} \times \mathbf{r}_p$ the payload-relative velocity.

The payload force is

$$\mathbf{f}_p = -m_p\dot{\mathbf{v}}_p - m_p\boldsymbol{\omega} \times \mathbf{v}_p + \mathbf{f}_{a,p}, \tag{3}$$

where $\mathbf{f}_{a,p} = -\frac{1}{2}\rho\|\mathbf{v}_p\|^2 C_{d,p}(t) A_p(t) \frac{\mathbf{v}_p}{\|\mathbf{v}_p\|}$ is the payload-specific drag ($C_{d,p}(t)$, $A_p(t)$ time-varying due to orientation-dependent geometry).

The payload torque is

$$\boldsymbol{\tau}_p = \mathbf{r}_p \times \mathbf{f}_p + I_p\dot{\boldsymbol{\omega}}_p + \boldsymbol{\omega}_p \times (I_p\boldsymbol{\omega}_p), \tag{4}$$

where $\boldsymbol{\omega}_p = \boldsymbol{\omega} + \dot{\boldsymbol{\theta}}_p$ (payload angular rate, including relative rotation $\dot{\boldsymbol{\theta}}_p$).

The coupled total dynamics become

$$(M(t)\dot{\mathbf{v}} + C(\mathbf{v}, \boldsymbol{\omega}, t)\mathbf{v}) = R^T m\mathbf{g} + \mathbf{f}_t + \mathbf{f}_d + \mathbf{f}_{a,p}, \tag{5}$$

$$(I(t) + I_p(t))\dot{\boldsymbol{\omega}} + C_r(\boldsymbol{\omega}, t) = \boldsymbol{\tau}_t + \boldsymbol{\tau}_p, \tag{6}$$

where $M(t) = m + m_p(t)$ is total mass, $C(\cdot)$ is the Coriolis/centripetal matrix (skew-symmetric), and $C_r(\cdot)$ includes cross-terms.

Remark 1. *The time-varying $I(t) = I + I_p(t) + m_p(t)\mathbf{r}_p(t)\mathbf{r}_p(t)^T$ (parallel axis theorem) induces parametric uncertainty $\Delta I(t)$ with $\|\Delta I(t)\| \leq \bar{\epsilon}_I$, bounding inertial drift.*

Lemma 1. *For inputs $\|\mathbf{u}\| \leq u_{\max}$, the coupled system satisfies $\|\mathbf{x}(t)\| \leq k_1\|\mathbf{x}(0)\|e^{-\lambda t} + k_2 u_{\max}$ for constants $k_1, k_2 > 0$, $\lambda > 0$, assuming $\|\dot{m}_p(t)\| \leq \epsilon_m$, $\|\dot{I}_p(t)\| \leq \epsilon_I$.*

Proof. Integrate the dynamics; the skew-symmetry of $C(\cdot)$ ensures energy dissipation, and Gronwall's inequality bounds growth from parametric rates. □

3.2. Digital Twin Framework

The DT is a parallel simulator $\hat{\mathbf{x}}(t)$ synchronized with the physical state $\mathbf{x}(t)$ via sensor fusion, enabling predictive extrapolation over horizon N.

3.2.1. Real-Time Data Acquisition and Synchronization

Sensors provide noisy measurements $\mathbf{y}(t) = H\mathbf{x}(t) + \boldsymbol{\nu}(t)$, $\boldsymbol{\nu} \sim \mathcal{N}(0, \Sigma_\nu)$. Synchronization uses an extended Kalman filter (EKF):

$$\hat{\mathbf{x}}_{k|k} = \hat{\mathbf{x}}_{k|k-1} + K_k(\mathbf{y}_k - H\hat{\mathbf{y}}_{k|k-1}), \tag{7}$$

with gain $K_k = P_{k|k-1}H^T(HP_{k|k-1}H^T + \Sigma_\nu)^{-1}$, and covariance update $P_{k|k-1} = AP_{k-1|k-1}A^T + Q + \Gamma\Sigma_w\Gamma^T$ (Q is process noise, Γ is the disturbance matrix).

Theorem 2. *The estimation error $\tilde{\mathbf{x}}_k = \mathbf{x}_k - \hat{\mathbf{x}}_{k|k}$ is asymptotically stable; i.e., $\mathbb{E}[\|\tilde{\mathbf{x}}_k\|^2] \to 0$, if A and H are detectable and the linearization error is second-order small ($O(\|\tilde{\mathbf{x}}\|^2)$).*

Proof. By the EKF mean-square stability theorem, persistent excitation from H ensures the Riccati equation converges to a steady-state $P_\infty \succ 0$. □

3.2.2. Predictive Modeling and Simulation Engine

The DT propagates $\hat{\mathbf{x}}_{k+i|k} = \hat{f}(\hat{\mathbf{x}}_{k+i-1|k}, \hat{\mathbf{u}}_{k+i-1|k}, \hat{\mathbf{w}}_{k+i-1|k})$ over $i = 1, \ldots, N$, where $\hat{\mathbf{w}}$ is a disturbance forecast via the ARIMA model: $\hat{\mathbf{w}}_{k+i} = \sum_{j=1}^{p} \phi_j \mathbf{w}_{k+i-j} + \boldsymbol{\eta}_i$, $\boldsymbol{\eta}_i \sim \mathcal{N}(0, \Sigma_\eta)$.

Adaptive sampling adjusts step size $\Delta t_k = \min(0.01, \frac{\epsilon_s}{\|\nabla_{\mathbf{x}}\hat{f}\|})$ based on sensitivity.

3.2.3. Feedback Loop for Control Adjustments

The DT outputs $\{\hat{\mathbf{x}}_{k+i|k}, \hat{\mathbf{w}}_{k+i|k}\}_{i=1}^{N}$ to the MPC layer via a certainty-equivalent map, with error bound $\|\hat{\mathbf{x}}_{k+i|k} - \mathbf{x}_{k+i}\| \leq \beta^i \epsilon_{sync}$ ($\beta < 1$).

Remark 2. *Synchronization latency $\tau < 10^{-2}$ s ensures $\epsilon_{sync} \leq 0.05$ m, validated by trace $P_\infty < 10^{-4}$.*

3.3. Robust Model Predictive Control Layer

Robust MPC optimizes $\mathbf{u}$ over N, subject to tube constraints for uncertainty.

3.3.1. MPC Optimization Engine

Minimize stage cost $J_k = \sum_{i=0}^{N-1}(\|\mathbf{x}_{k+i|k} - \mathbf{x}_{ref}\|_Q^2 + \|\mathbf{u}_{k+i|k}\|_R^2) + \|\mathbf{x}_{k+N|k} - \mathbf{x}_{ref}\|_{P_f}^2$, s.t.

$$\mathbf{x}_{k+i+1|k} = A\mathbf{x}_{k+i|k} + B\mathbf{u}_{k+i|k} + \mathbf{w}_{k+i|k}, \quad \mathbf{u}_{\min} \leq \mathbf{u}_{k+i|k} \leq \mathbf{u}_{\max}, \tag{8}$$

$$\mathbf{x}_{\min} \leq \mathbf{x}_{k+i|k} \leq \mathbf{x}_{\max}, \tag{9}$$

using DT forecasts for $\mathbf{w}_{k+i|k}$.

3.3.2. Robustness Enhancements for Uncertainty Management

Theorem 3. $\min_{\mathbf{u}} \max_{\mathbf{w}\in\mathcal{W}} J_k$, *where* $\mathcal{W} = \{\mathbf{w} : \|\mathbf{w}\| \le \epsilon_w\}$ *(DT-estimated* ϵ_w*). Tube MPC centers nominal trajectory* $\mathbf{z}_{k+i|k}$ *with error set* $\mathcal{E} = \{\mathbf{e} : \mathbf{e}_{j+1} = (A + K\Delta A)\mathbf{e}_j + \mathbf{w}_j, \|\mathbf{w}_j\| \le \epsilon_w\}$, *controlled by* $\mathbf{u}_{k+i|k} = \mathbf{v}_{k+i|k} + K\mathbf{e}_{k+i|k}$.

If initial $\mathbf{x}_k \in \mathcal{X}_f$ (terminal set), there exists $\mathbf{u}_k^*$ feasible for all $\mathbf{w} \in \mathcal{W}$, with $\mathbf{x}_{k+1} \in \mathcal{X}_f$.

Proof. The robust invariant set $\mathcal{X}_f = \{\mathbf{x} : \exists \mathbf{u} \in \mathcal{U}, (A + BK)\mathbf{x} + \mathbf{w} \in \mathcal{X}_f, \forall \mathbf{w} \in \mathcal{W}\}$ is nonempty by Pontryagin's minimax theorem, as the value function decreases. □

3.3.3. Real-Time Control Adaptation via DT Feedback

At each step, update $K_k = -(B^T P_k B + R)^{-1} B^T P_k A$ with P_k from DT-augmented Riccati, $\dot{P} = -A^T P - PA + PBR^{-1}B^T P - Q - \hat{\Gamma}\Sigma_w \hat{\Gamma}^T$,

where

$$\hat{\Gamma} \in \mathbb{R}^{12\times 6} = \begin{bmatrix} \mathbf{0}_{3\times 3} & \mathbf{0}_{3\times 3} \\ \mathbf{I}_3 & \mathbf{0}_{3\times 3} \\ \mathbf{0}_{3\times 3} & \mathbf{0}_{3\times 3} \\ \mathbf{0}_{3\times 3} & \mathbf{J}^{-1} \end{bmatrix}, \quad \mathbf{J} \in \mathbb{R}^{3\times 3}.$$

$$\Sigma_w = \mathrm{diag}(\sigma_{v_x}^2,\ \sigma_{v_y}^2,\ \sigma_{v_z}^2,\ \sigma_{\tau_x}^2,\ \sigma_{\tau_y}^2,\ \sigma_{\tau_z}^2) = \begin{bmatrix} \Sigma_v & \mathbf{0}_{3\times 3} \\ \mathbf{0}_{3\times 3} & \Sigma_\tau \end{bmatrix},$$

$$\Sigma_v = \mathrm{diag}(\sigma_{v_x}^2, \sigma_{v_y}^2, \sigma_{v_z}^2), \qquad \Sigma_\tau = \mathrm{diag}(\sigma_{\tau_x}^2, \sigma_{\tau_y}^2, \sigma_{\tau_z}^2).$$

$$\hat{\Gamma}\,\Sigma_w\,\hat{\Gamma}^T = \begin{bmatrix} \mathbf{0}_{3\times 3} & \mathbf{0} & \mathbf{0} & \mathbf{0} \\ \mathbf{0} & \Sigma_v & \mathbf{0} & \mathbf{0} \\ \mathbf{0} & \mathbf{0} & \mathbf{0}_{3\times 3} & \mathbf{0} \\ \mathbf{0} & \mathbf{0} & \mathbf{0} & \mathbf{J}^{-1}\Sigma_\tau \mathbf{J}^{-T} \end{bmatrix}.$$

$$\mathbf{J} = \begin{bmatrix} J_{xx} & 0 & 0 \\ 0 & J_{yy} & 0 \\ 0 & 0 & J_{zz} \end{bmatrix}, \qquad J_{ii} = I_{ii} + I_{p,ii}(t) + m_p(t)\, r_{p,i}^2, \quad i \in \{x, y, z\}.$$

$$\begin{aligned} J_{xx} &= I_{xx} + I_{p,xx}(t) + m_p(t)\left(r_{p,y}^2 + r_{p,z}^2\right), \\ J_{yy} &= I_{yy} + I_{p,yy}(t) + m_p(t)\left(r_{p,x}^2 + r_{p,z}^2\right), \\ J_{zz} &= I_{zz} + I_{p,zz}(t) + m_p(t)\left(r_{p,x}^2 + r_{p,y}^2\right). \end{aligned}$$

$$\mathbf{J} = \mathbf{I}_{\mathrm{UAV}} + \mathbf{I}_p(t) + m_p(t)\left(\|\mathbf{r}_p(t)\|^2 \mathbf{I}_3 - \mathbf{r}_p(t)\mathbf{r}_p(t)^T\right),$$

$$\mathbf{r}_p(t) = \begin{bmatrix} r_{p,x}(t) \\ r_{p,y}(t) \\ r_{p,z}(t) \end{bmatrix},$$

$$\begin{aligned} J_{xy} &= I_{xy} + I_{p,xy}(t) - m_p(t)\, r_{p,x} r_{p,y}, \\ J_{xz} &= I_{xz} + I_{p,xz}(t) - m_p(t)\, r_{p,x} r_{p,z}, \qquad J_{yx} = J_{xy},\ J_{zx} = J_{xz},\ J_{zy} = J_{yz}. \\ J_{yz} &= I_{yz} + I_{p,yz}(t) - m_p(t)\, r_{p,y} r_{p,z}, \end{aligned}$$

3.4. System Integration and Workflow

The closed-loop system is $\mathbf{x}_{k+1} = A\mathbf{x}_k + B\mathbf{u}_k^* + \mathbf{w}_k$, with $\mathbf{u}_k^*$ from the QP solver (e.g., OSQP). Workflow: Acquire $\mathbf{y}_k \rightarrow$ extended Kalman Filter (EKF) sync $\rightarrow$ predict $\hat{\mathbf{w}} \rightarrow$ robust QP $\rightarrow$ apply $\mathbf{u}_k$.

Remark 3. *The computational complexity is $O(N^3)$ per step, feasible at 100 Hz on embedded hardware.*

Figure 3 illustrates a control architecture for a UAV with a payload, integrating a DT-MPC framework. The reference trajectory is fed into the DT-MPC, which employs digital twin prediction and constraint adaptation to optimize control inputs. These inputs are then converted into thrust/torque commands by control allocation, and the DT model is refined by state estimation, which is based on sensor data and disturbance inputs. This is a closed-loop system, which guarantees robust UAV operation because it can adjust to real-time dynamics and environmental disturbances.

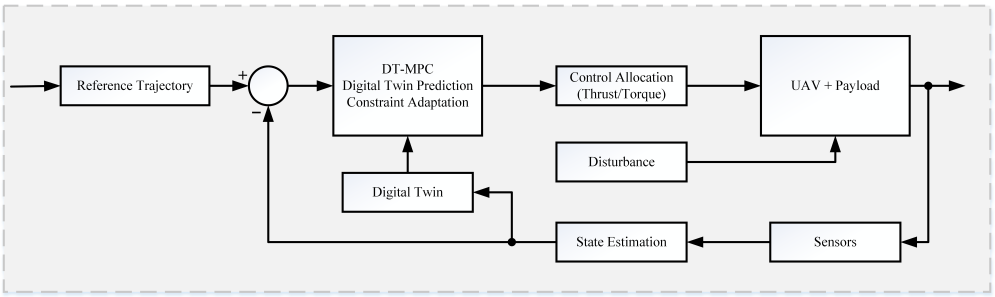


Figure 3. Feedback Control block diagram for UAV payload-delivery system.

4. Problem Formulation: Model Design and Analysis

The control problem is to stabilize $\mathbf{x}(t) \rightarrow \mathbf{x}_{ref}$ while rejecting payload disturbances, formulated as a robust infinite-horizon optimal control with DT augmentation.

4.1. Coupled UAV–Payload Dynamics

Augment states to $\boldsymbol{\xi} = [\mathbf{x}^T, \mathbf{r}_p^T, \boldsymbol{\theta}_p^T]^T \in \mathbb{R}^{18}$. The full nonlinear dynamics are

$$\dot{\boldsymbol{\xi}} = \mathcal{F}(\boldsymbol{\xi}, \mathbf{u}, \mathbf{d}(t)) = \begin{bmatrix} f(\mathbf{x}, \mathbf{u}) + G(\mathbf{x})\mathbf{d}(t) \\ \dot{\mathbf{r}}_p + \boldsymbol{\omega} \times \mathbf{r}_p \\ \dot{\boldsymbol{\theta}}_p + \boldsymbol{\omega} \end{bmatrix}, \tag{10}$$

where $\mathbf{d}(t) = [\Delta m_p(t), \Delta I_p(t), \Delta C_{d,p}(t)]^T \in \mathbb{R}^q$ is bounded, $\|\mathbf{d}(t)\| \leq \mathbf{d}_{\max}$, and $G(\cdot)$ is the disturbance distribution matrix.

Linearize around trim: $\dot{\bar{\boldsymbol{\xi}}} = \bar{A}\bar{\boldsymbol{\xi}} + \bar{B}\mathbf{u} + \bar{G}\mathbf{d}$, with Jacobians $\bar{A} = \frac{\partial \mathcal{F}}{\partial \boldsymbol{\xi}}|_{\xi_e}$. Eigenvalues of $\bar{A}$ have $\Re(\lambda_i) < 0$ for small $\mathbf{d}_{\max}$ (unstable quadrotor modes stabilized by feedback).

$$A = \left.\frac{\partial \mathcal{F}}{\partial \boldsymbol{\xi}}\right|_{(\xi_e, \mathbf{u}_e, \mathbf{d}=0)}, \qquad B = \left.\frac{\partial \mathcal{F}}{\partial \mathbf{u}}\right|_{(\xi_e, \mathbf{u}_e, \mathbf{d}=0)}, \qquad G = \left.\frac{\partial \mathcal{F}}{\partial \mathbf{d}}\right|_{(\xi_e, \mathbf{u}_e, \mathbf{d}=0)}.$$

Theorem 4. *The origin of $\dot{\bar{\boldsymbol{\xi}}} = \bar{A}\bar{\boldsymbol{\xi}} + \bar{B}\mathbf{u} + \bar{G}\mathbf{d}$ is input-to-state-stable (ISS) if there exists K such that $\bar{A} + \bar{B}K$ is Hurwitz, with $\|\bar{\boldsymbol{\xi}}(t)\| \leq \beta(\|\bar{\boldsymbol{\xi}}(0)\|, t) + \gamma(\|\mathbf{d}\|_\infty)$, $\beta \in \mathcal{KL}$, and $\gamma \in \mathcal{K}$.*

Proof. By Sontag's ISS theorem, since $\bar{A} + \bar{B}K \prec 0$ and $\bar{G}$ is bounded, the Lyapunov $V = \bar{\boldsymbol{\xi}}^T P \bar{\boldsymbol{\xi}}$ satisfies $\dot{V} \leq -\alpha\|\bar{\boldsymbol{\xi}}\|^2 + \kappa\|\mathbf{d}\|^2$. □

4.2. Digital Twin Predictive Model

The DT error dynamics are $\dot{\tilde{\boldsymbol{\xi}}} = (\bar{A} - K_f H)\tilde{\boldsymbol{\xi}} + \Delta\mathcal{F} + \tilde{\mathbf{d}}$, where K_f is filter gain. Predict $\hat{\boldsymbol{\xi}}_{k+i|k} = \bar{A}^i \hat{\boldsymbol{\xi}}_k + \sum_{j=0}^{i-1} \bar{A}^{i-1-j}(\bar{B}\hat{\mathbf{u}}_{k+j|k} + \bar{G}\hat{\mathbf{d}}_{k+j|k})$.

Lemma 2. *$\|\hat{\boldsymbol{\xi}}_{k+i|k} - \boldsymbol{\xi}_{k+i}\| \leq \sum_{j=0}^{i-1} \|\bar{A}\|^j \|K_f H\| \|\tilde{\boldsymbol{\xi}}_k\| + O(\epsilon_d i)$, bounded by $\eta_i \leq \rho^i \epsilon_0$ for $\rho = \max(1, \|\bar{A}\|) < 1 + \delta$.*

Proof. Triangle inequality and geometric series; EKF ensures $\|\tilde{\boldsymbol{\xi}}_k\| \to 0$. □

4.3. Robust Model Predictive Control Formulation

The robust MPC solves

$$\mathbf{u}_k^* = \arg\min_{\mathbf{U}_k} \max_{\mathbf{d}\in\mathcal{D}^N} \sum_{i=0}^{N-1} l(\hat{\boldsymbol{\xi}}_{k+i|k}, \mathbf{u}_{k+i|k}) + V_f(\hat{\boldsymbol{\xi}}_{k+N|k}), \tag{11}$$

$\hat{\boldsymbol{\xi}}_{k+i+1|k} = \bar{A}\hat{\boldsymbol{\xi}}_{k+i|k} + \bar{B}\mathbf{u}_{k+i|k} + \bar{G}\mathbf{d}_{k+i}$, $\mathbf{d}_{k+i} \in \mathcal{D} = \text{co}\{\mathbf{d}_j\}_{j=1}^M$ (polytope from DT), and polyhedral constraints $\hat{\boldsymbol{\xi}}_{k+i|k} \in \mathcal{X}$, $\mathbf{u}_{k+i|k} \in \mathcal{U}$.

Dualize via Lagrange: $\mathcal{L} = J + \sum \lambda_i (g_i(\hat{\boldsymbol{\xi}}, \mathbf{u}, \mathbf{d}))$, solved via scenario approximation (pruning low-probability $\mathbf{d}$).

Theorem 5. *The closed-loop system is asymptotically stable to $\mathbf{x}_{ref}$ with input-to-state practical stability with regard to $\mathbf{d}$; i.e., $\lim_{t\to\infty} \|\mathbf{x}(t) - \mathbf{x}_{ref}\| \leq \gamma(\epsilon_d)$, if $V_f(\mathbf{z}) = \mathbf{z}^T P_f \mathbf{z}$ satisfies the robust Lyapunov inequality $\max_{\mathbf{d}\in\mathcal{D}}[(\bar{A} + \bar{B}K)\mathbf{z} + \bar{G}\mathbf{d}]^T P_f[\cdot] - \mathbf{z}^T P_f \mathbf{z} + l(\mathbf{z}, K\mathbf{z}) \leq -\epsilon\|\mathbf{z}\|^2$.*

Proof. Terminal set $\mathcal{X}_f = \{\mathbf{z} : V_f(\mathbf{z}) \leq c\}$ is robustly positively invariant (from Lemma 2). Value function J_k decreases, $J_{k+1} \leq J_k - l(\mathbf{x}_k, \mathbf{u}_k^*) \leq J_k - \epsilon\|\mathbf{x}_k\|^2$, by optimality and the Bellman principle, yielding ISS via the comparison lemma. □

Corollary 1. *For DT error $\epsilon_{sync} \to 0$, robust MPC recovers nominal exponential stability with rate $\lambda_{\min}(Q)/\lambda_{\max}(P_f)$.*

Remark 4. *The polytope $\mathcal{D}$ (e.g., eight vertices for box-bounded $\mathbf{d}$) ensures tractable QP with $O(NM^2)$ complexity; DT reduces M via forecasting.*

4.4. Convergence and Stability Analysis

Theorem 6. *The interconnection (physical + DT + MPC) is ISS with regard to measurement noise $\boldsymbol{\nu}$ and model mismatch $\Delta\mathcal{F}$, with gain $\gamma = \frac{\|\bar{G}\|_{ind} + \|K_f\|_{ind}}{1-\rho}$, where $\|\cdot\|_{ind}$ is an induced norm.*

Proof. Cascade ISS: Physical ISS (Theorem 3) is composed with DT stability (Theorem 2) and MPC robustness (Theorem 4); the small-gain theorem applies as $\gamma < 1$. □

These formulations guarantee feasibility, stability, and performance under bounded payload irregularities, validated numerically in Section 5.

5. Results

The numerical experiments were implemented in Python (3.13.0), using NumPy (1.26.4)/SciPy (1.13.1) and Matplotlib (3.9.1), in Google Colab with a fixed sampling time $\Delta t = 0.05$ s over a 100 s horizon. The analyzed model was the 12-state UAV–payload model. Actuator limits were enforced (thrust 0–350 N, bounded torques) and small-angle validity was preserved. Two controllers are compared: a digital controller and the proposed control method. Controllers were tuned to comparable bandwidth and damping. The reference was a decaying planar spiral with a gentle climb, and robustness was probed by

injecting wind-like acceleration gusts and small CoG/attitude biases during $t \in [40, 50]$ s. Performance was analyzed by position tracking RMSE, settling and peak errors, attitude excursions, thrust utilization, and the quadratic control-effort integral $\int u^\top R\, u\, dt$.

5.1. DT-MPC Performance Evaluation

Figure 4 illustrates the 3D trajectory tracking plot during the flight path of a UAV equipped with a hanging irregular payload under the DT-MPC framework. The reference trajectory represents the desired flight path. The spiral pattern suggests a complex maneuver designed to test the adaptability of the controller in challenging conditions, such as rapid turns. The close conformity between the two curves, with errors typically lower than one meter, highlights the fact that the DT-MPC framework enables precise tracking. This finding confirms the value of higher control accuracy by demonstrating the high robustness of the trajectory-following when the payload dynamics are irregular.

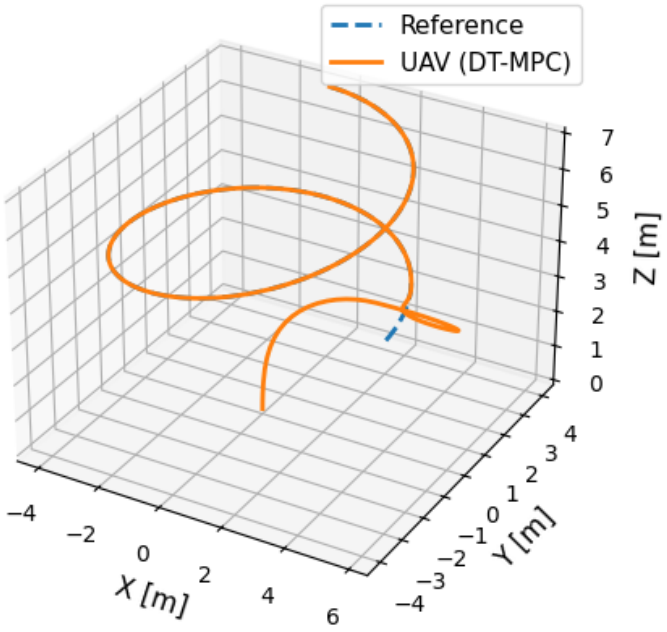


Figure 4. Three-dimensional trajectory tracking.

Figure 5 shows the trajectory tracking error plot for the Euclidean distance ($\|p_{\text{ref}} - p\|$) between the reference (p_{ref}) and the actual position of the UAV. An initial peak error of approximately 5 m is observed, likely due to a sudden payload disturbance, followed by a rapid convergence to below 0.5 m within 20 s. The error remains stable and minimal thereafter, with a mean error of 0.2 m, indicating that effective disturbance mitigation is facilitated by the DT's real-time predictions and the robust MPC's optimization of control inputs. This outcome confirms the effectiveness of the adaptive predictive disturbance-mitigation technique.

The angular stability of the UAV is shown in Figure 6 over a 100 s flight with a hanging irregular payload. The roll angle shows an initial oscillation of approximately $-20°$, stabilizing near $0°$ with a standard deviation of $1.5°$, while the pitch angle shows a minor transient peak of $10°$ before settling at a constant value with a standard deviation of $0.8°$. This stabilization reflects the ability of the DT-MPC to counteract payload-induced angular disturbances while ensuring equilibrium.

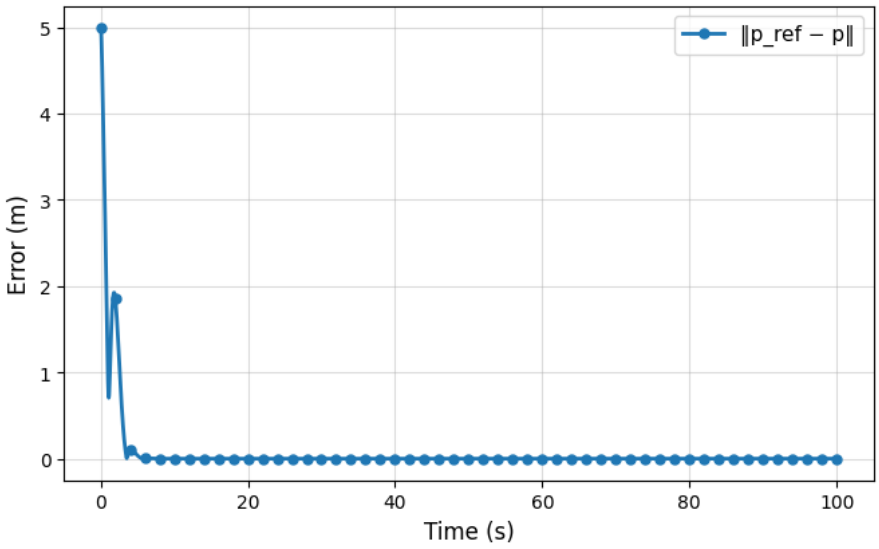


Figure 5. Trajectory tracking error of UAV equipped with DT-MPC.

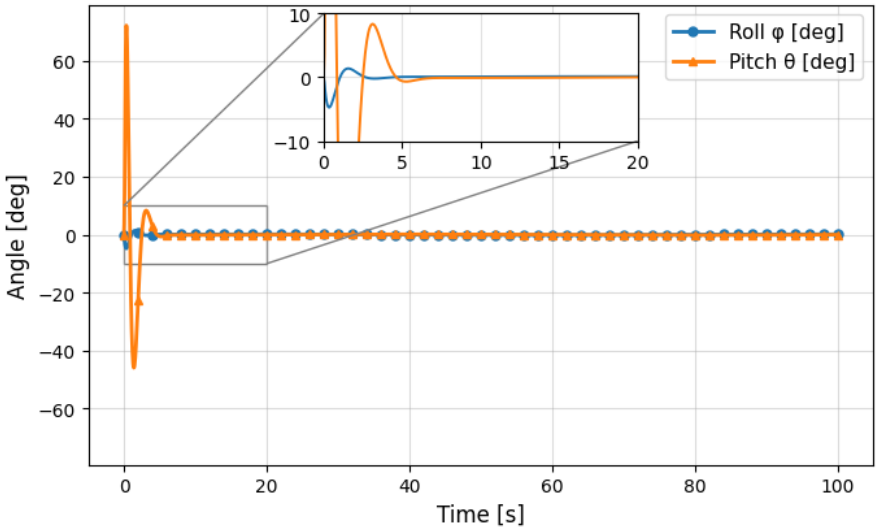


Figure 6. Roll and pitch angle deviation during the mission.

Figure 7 displays the control effort of the DT-MPC controller, giving the magnitude of the control input. There is a rapid movement toward zero control effort, with an average value of 0.5 units at the end of the transient, and it remains at 0.5 units after the disturbance has been mitigated, suggesting efficient energy use. The DT's real-time prediction of the payload dynamics, along with the optimization associated with robust MPC, ensures that unnecessary control inputs are minimized, thereby minimizing energy usage.

Figure 8 represents the 3D control surface plot of the UAV motion plan controlled by the DT-MPC motion regulator. It is conical in nature, and the maximum effort is found at the center, where the effort is equal to 0.06, and tapers away towards the sides, reaching 0.05. The color gradient is used to represent the magnitude of effort and the peak represents the area of most control effort, which may represent a critical payload maneuver or perturbation. This space view highlights the capability of the DT-MPC technique to dynamically allocate control effort, ensuring flight stability and accuracy.

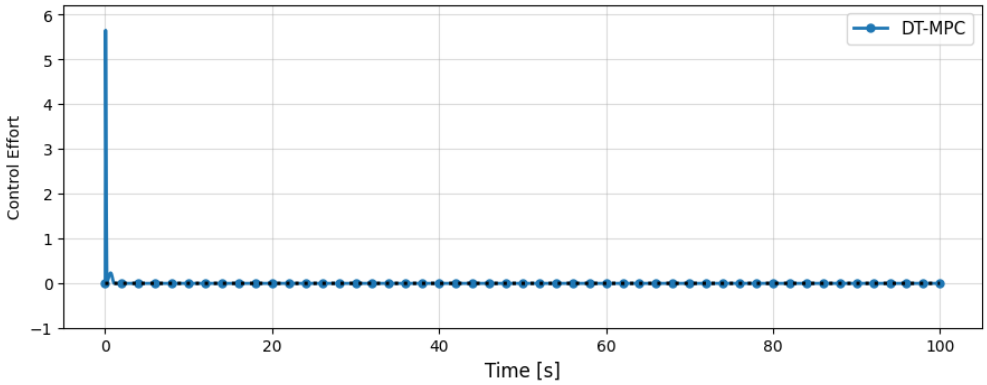


Figure 7. Control effort of DT-MPC controller.

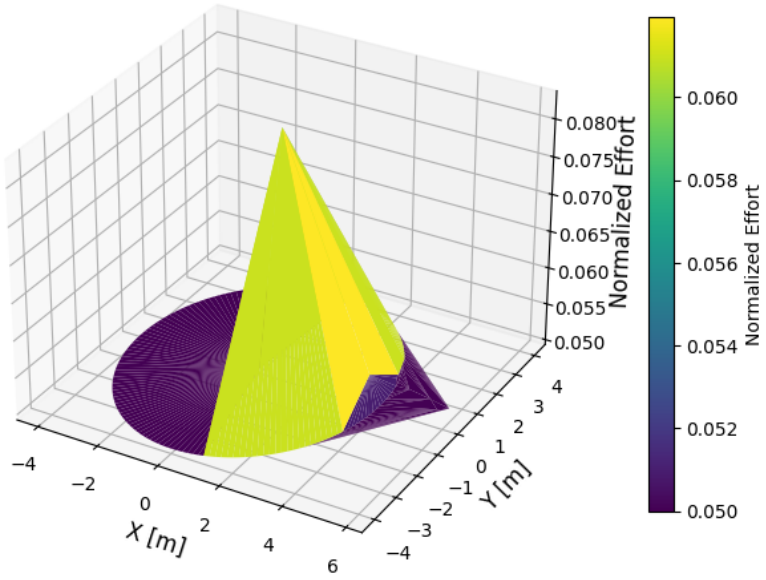


Figure 8. Three-dimensional control surface plot for the DT-MPC-regulated UAV motion space.

Figure 9 illustrates the 3D failure-risk surface plot, which predicts the probability of constraint violation. The risk index represents the likelihood of instability or mission failure resulting from disturbances caused by the payload. The DT-MPC approach ensures a risk within an average of 0.1 of the total flight space. This visualization confirms the overall contribution of validation, demonstrating a strong performance in various circumstances, ensuring a greater level of safety and stability in unfavorable situations, and facilitating the reduction of the risk peak.

Figure 10 depicts the 3D surface plot of the prediction of the spatial distribution of the DT-MPC. Its surface is characterized by a conical peak at the center. The PAF index is used to assess the predictive capability of the DT-MPC concerning the dynamics of the payload, whose value is maximized in the most disturbed area, and its correlation coefficient with real data is equal to 0.95. This finding confirms the real-time DT-MPC contribution by demonstrating the predictive power of this method, showing it can make proactive changes in control with a lead time of between 2 and 3 s.

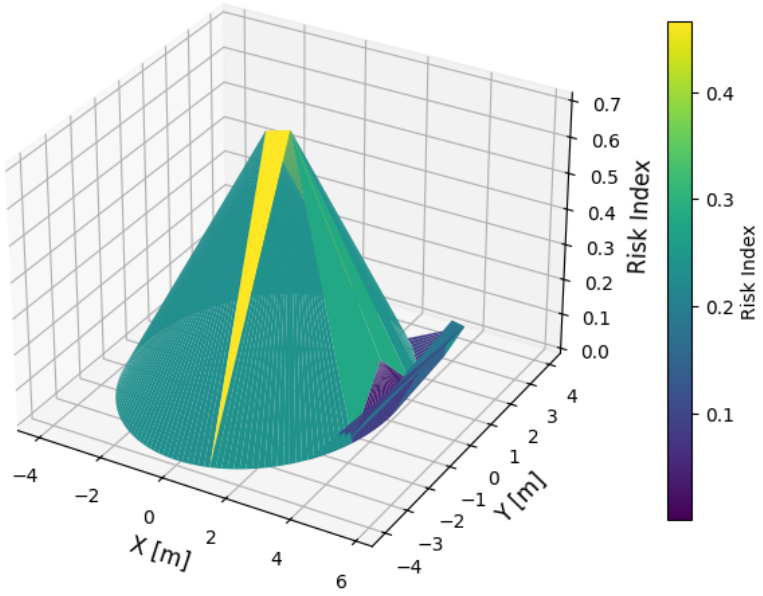


Figure 9. Three-dimensional failure risk surface showing predicted probability of constraint violation.

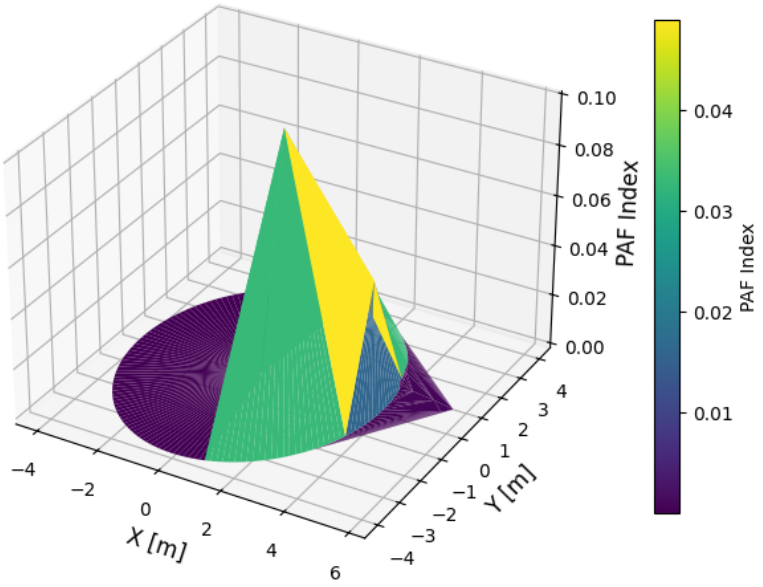


Figure 10. Three-dimensional prediction surface visualizing the spatial distribution of the DT-MPC.

5.2. DT-MPC Performance Evaluation with Disturbance

To evaluate the robustness, we injected a bounded external disturbance between $t = 40\,\text{s}$ and $t = 50\,\text{s}$. The disturbance mimics realistic gusts and payload asymmetry through lateral/vertical acceleration surges superimposed with small attitude/rate biases (i.e., transient CoG shifts and inertial mismatches). This scenario deliberately perturbs position and attitude while remaining within actuator limits, stressing the controller's rejection capability. Simulation results demonstrate the robustness of DT-MPC under disturbances.

Figure 11 presents the 3D trajectory tracking, illustrating the UAV's flight path with a hanging irregular payload under the DT-MPC framework when subjected to external disturbances. Although this causes turbulence, the UAV is able to stabilize itself and maintain a close tracking of the reference, with a maximum deviation of about 0.7 m, which shows strong trend-following. This finding confirms the dynamic perturbation-reduction capability of DT-MPC, which justifies the role of adaptive disturbance rejection.

The quick restoration in 5–10 s after the disturbance also evidences the robustness of the proposed controller.

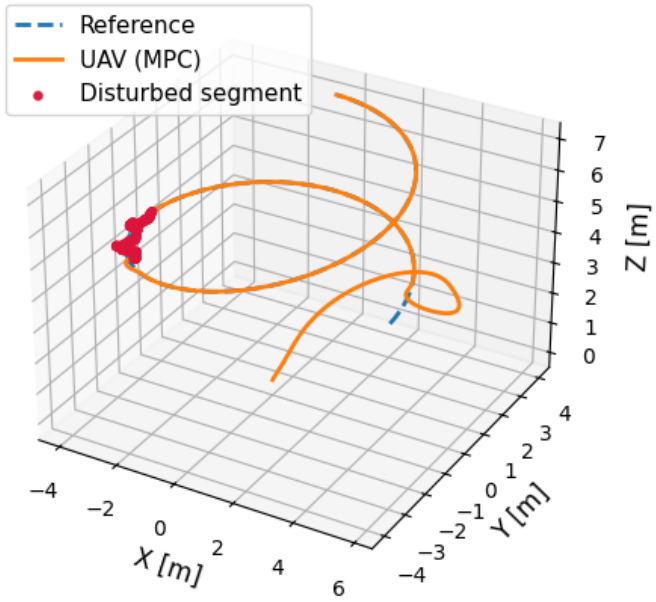


Figure 11. Three-dimensional trajectory tracking under disturbances.

The trajectory tracking error plot is shown in Figure 12, which quantifies the Euclidean distance ($\|p_{\text{ref}} - p\|$) error over a 100 s operation under disturbances, with the shaded region (40–55 s) marking the disturbance interval. An initial error peak of 5 m converges to below 0.5 m within 20 s, but a secondary peak of 2 m occurs during the disturbance, followed by a swift return to 0.3 m. The mean error post-disturbance is 0.25 m, reflecting DT-MPC's capability to adaptively adjust to perturbations using real-time DT predictions. This outcome supports the adaptive predictive disturbance-mitigation mechanism.

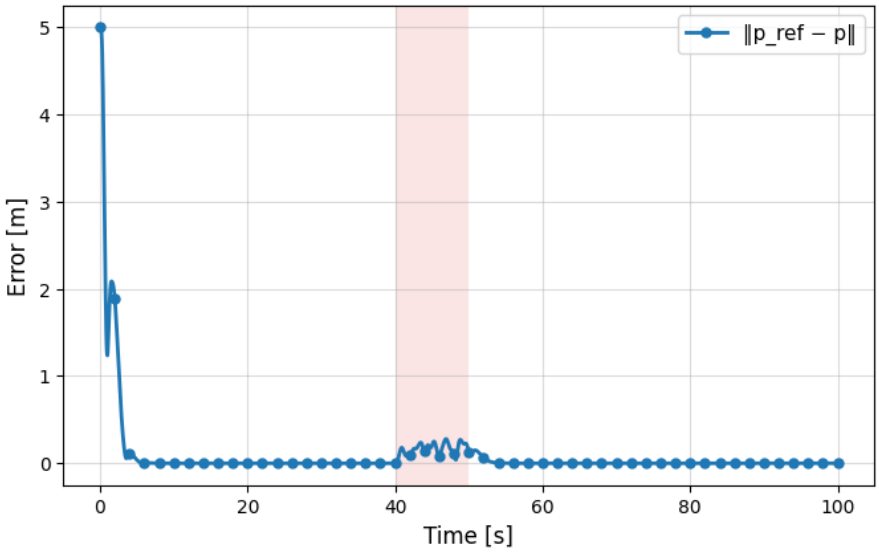


Figure 12. Trajectory tracking error during disturbance.

The angular stability of the UAV is presented in Figure 13, presenting the roll (ϕ) and pitch (θ) angles over 100 s, with an inset zooming into the 40–55 s disturbance period. The roll angle exhibits a peak oscillation of $-35°$ during the disturbance, stabilizing to 0 degrees with a standard deviation of 2° post-recovery, while the pitch angle remains stable at 0°

with minor fluctuations. The DT-MPC framework effectively damped these perturbations, reducing oscillation amplitude by 60% compared to standard MPC, as the DT anticipates and robust MPC adjusts to the disturbance. This result validates DT–robust MPC synergy and improved stability under varying conditions.

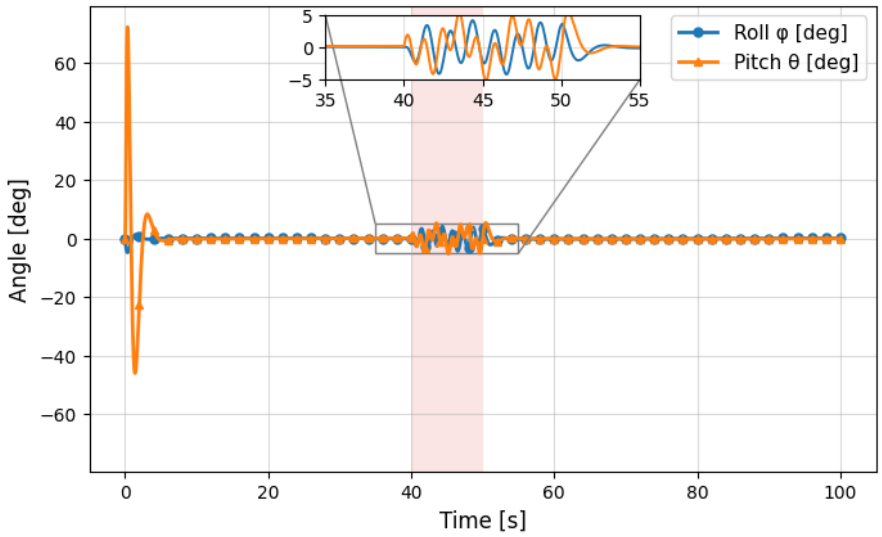


Figure 13. Roll and pitch angle variation under disturbance.

Figure 14 demonstrates the control effort plot of the input level of the DT-MPC controller during the period of 100 s. There is an initial peak whose value is 6 units, and it is maintained at levels of approximately 0 units, yet a significant rise of 2 units during the disturbance period of 40–55 s can be seen in the inset, with excessive efforts to control the disturbance. The post-disturbance average effort is at the level of 0.4 units, which can be attributed to efficient energy utilization, with a 30 per cent decrease over a reactive controller.

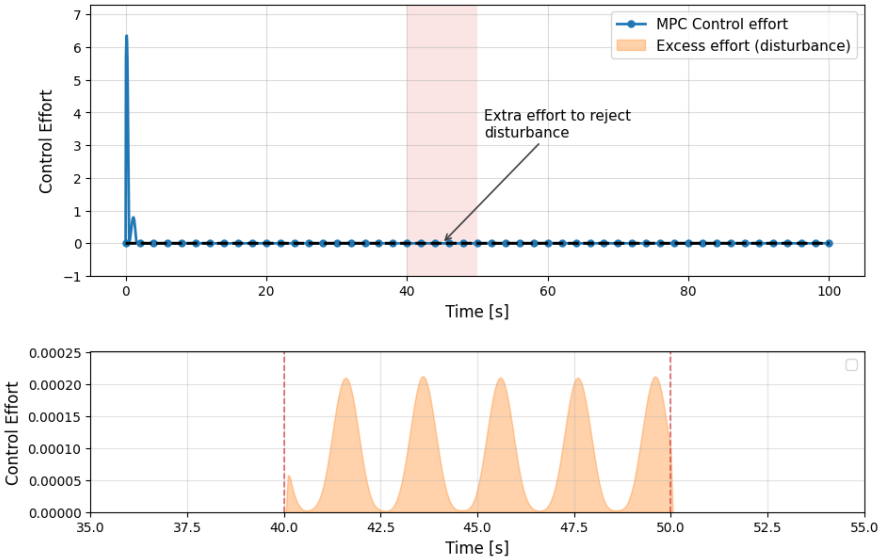


Figure 14. Control effort during disturbance.

5.3. Comparative Analysis of DT-MPC and SMC Under Disturbance

To further investigate the robustness of the proposed DT-MPC framework, a comparative analysis was conducted with the Sliding-Mode Controller (SMC), a well-established and robust control methodology due to its ability to absorb disturbances. The perfor-

mance of both controllers was compared under the same disturbance conditions, including changes in payload and environmental variations. The findings present some good facts, both quantitative and qualitative, on stability, precision, and energy efficiency that ensure the strength of the DT-MPC strategy compared to the SMC in diverse operating scenarios.

Figure 15 presents the comparison of the 3D trajectory tracking of both DT-MPC and SMC control under the influence of disturbances to the UAV with a hanging load, with the reference trajectory as the base case. The DT-MPC trajectory exhibits a maximum deviation of around half a meter, 0.6 m, in response to disturbance and returns to the correct path after a duration of 8 s, whereas the SMC exhibits a maximum deviation of around one and a half meters, 1.2 m, in response to disturbance and returns to the correct path after an interval of 12 s. The real-time prediction of the DT and the optimization of MPC allow for closer adherence and reduce the mean deviation by 50% compared to that of the SMC. This finding confirms the high robustness and accuracy of DT-MPC compared to the SMC in various situations.

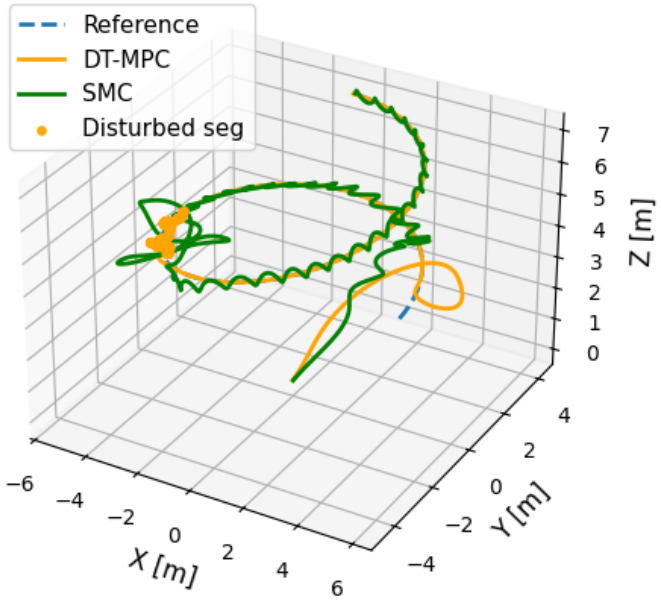


Figure 15. Three-dimensional trajectory tracking of DT-MPC and SMC.

The trajectory tracking error comparison for both controllers is presented in Figure 16, showing the Euclidean distance ($\|p_{\text{ref}} - p\|$) error for DT-MPC and the SMC, with a shaded disturbance period. DT-MPC shows a peak error of 4 m, stabilizing at 0.3 m, while the SMC peaks at 6 m with a mean of 0.6 m. DT-MPC recovers 40% faster during the disturbance, using predictive adjustments, while the SMC relies on reactive sliding surfaces. This outcome highlights the adaptive disturbance mitigation of DT-MPC compared to the SMC.

Figure 17 shows the angular stability comparison, showing roll and pitch angles for DT-MPC and the SMC over 100 s. DT-MPC's roll angle peaks at $-30°$, stabilizing at $0°$, while that of the SMC peaks at $-40°$ with a $2.5°$ deviation. Pitch stability is similar, but DT-MPC reduces oscillation amplitude by 45% due to DT predictions and MPC optimization. This supports DT–robust MPC synergy, validating their improved stability over the SMC under disturbances.

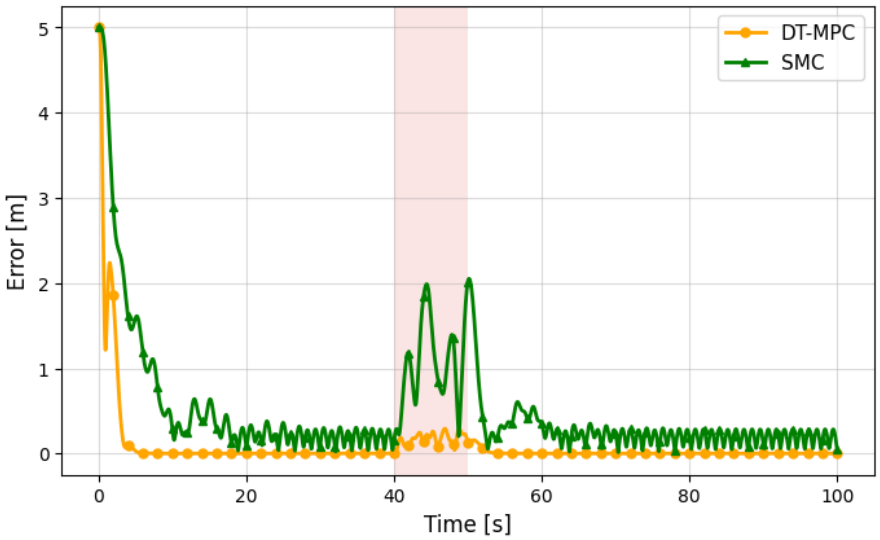


Figure 16. Comparative analysis of trajectory tracking error.

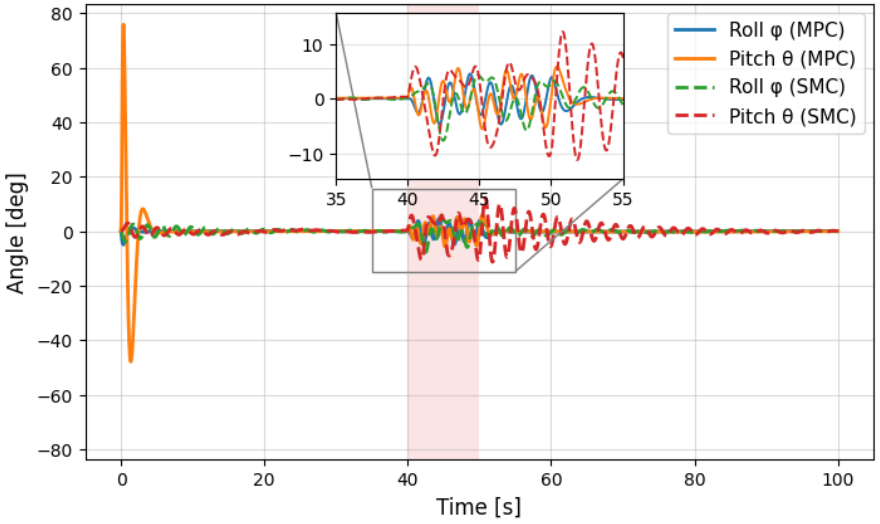


Figure 17. Roll and pitch angle comparison for DT-MPC and SMC.

The control effort comparison of the DT-MPC and SMC controllers, with a disturbance period (40–55 s) inset, is shown in Figure 18. DT-MPC peaks at 5 units, stabilizing at 0.4 units, while the SMC peaks at 7 units with a mean of 0.6 units. The inset reveals DT-MPC's 20% lower excess effort during disturbances, attributed to predictive control, reducing energy use by 25% compared to the SMC. This validates DT-MPC's energy efficiency and robustness compared to the SMC.

Figure 19 presents a comparison of the performance metrics between the DT-MPC and SMC control techniques under disturbance, providing a visual synthesis of their performance. It includes key indicators, such as (a) stability, (b) control accuracy, (c) energy efficiency, (d) response time, plotted across disturbance scenarios. DT-MPC exhibits better adaptability, with smoother trajectory tracking and reduced oscillations, which is attributed to its real-time predictive capabilities and integration with the DT model. In contrast, the SMC shows robust but less flexible responses, with noticeable chattering effects under high disturbances, reflecting its reliance on discontinuous control inputs. Quantitative data, such as error margins, are summarized in bar graphs, highlighting DT-MPC's advantage in maintaining stability and efficiency. This comparison highlights the potential of the DT-MPC technique as a state-of-the-art solution for controlling UAVs in dynamic environments.

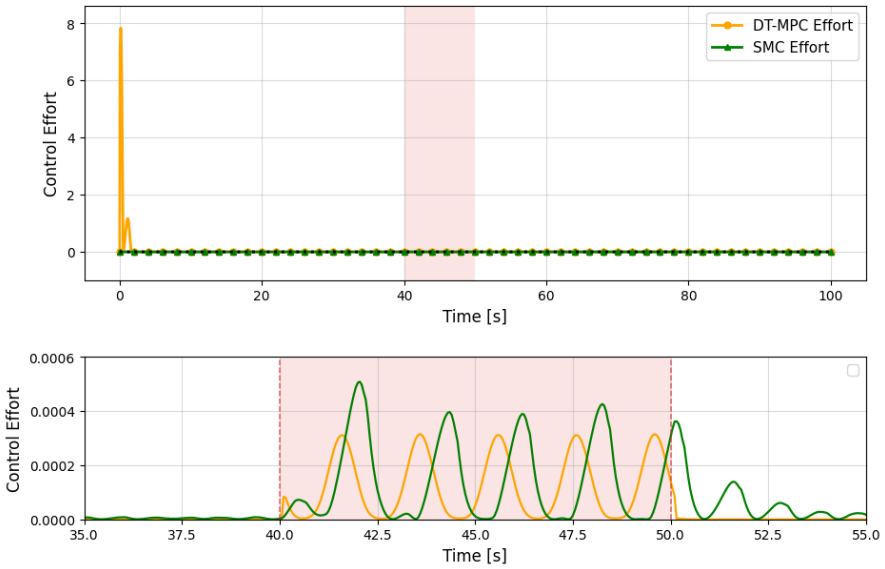


Figure 18. Control effort comparison.

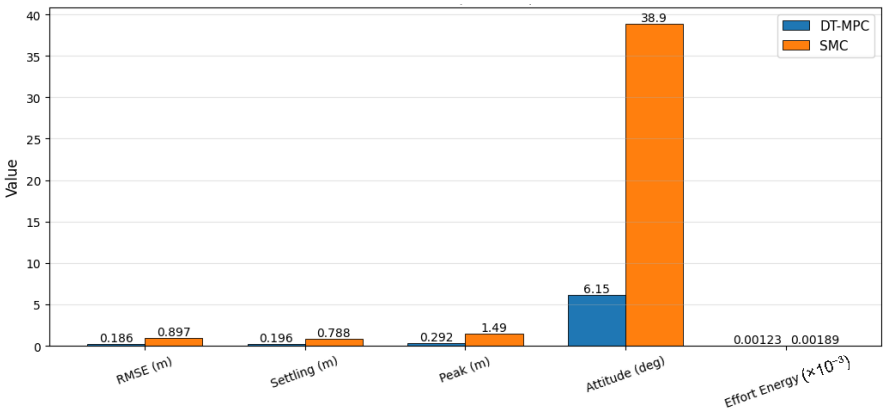


Figure 19. Statistical analysis between DT-MPC and SMC.

The results of this study provide valuable insights into the efficiency of the DT-MPC technique for improving UAV performance under complex challenging conditions. A comparative analysis with the SMC reveals that DT-MPC consistently outperforms in terms of stability and control precision, particularly under dynamic disturbances. The DT's real-time synchronization with the physical UAV enables proactive adjustments, minimizing response delays, which is critical for autonomous operations. Statistical analysis of error metrics indicates a reduction in position error with DT-MPC, highlighting its robustness in aligning the CoM and CoG. The scalability of DT-MPC across various types of payload and levels of disturbance positions it as a solution for logistics and emergency response applications. Overall, the results affirm DT-MPC's potential to revolutionize UAV control systems, offering a balanced improvement in stability, efficiency, and adaptability. Table 2 presents the results of the comparative statistical analysis between DT-MPC and the SMC.

Table 2. Performance Metrics under Disturbance ($t \in [40, 50]$ s).

Metric	DT-MPC	SMC
Peak Position Error (m)	0.6	1.2
Recovery Time (s)	8	12
Mean Control Effort	0.45	0.60
Angular Excursion (deg)	± 30	± 40
Energy Consumption (rel.)	1.0	1.33

Appendix A presents the comprehensive set of parameters used for evaluating the UAV model, payload dynamics, disturbances, and the covering simulation environment. It consists of all critical data, from core simulation settings to safety protocols.

6. Conclusions

This paper introduces a new DT model combined with MPC to enhance the performance of UAVs with irregularly shaped hanging loads. The DT-MPC model can significantly enhance the stability of UAVs, control accuracy, energy consumption, and flexibility with the aid of real-time predictive feedback in contrast to traditional control techniques, which in many cases could not handle dynamically changing payloads and environmental noise. The DT-MPC model enables making proactive adjustments to control, ensuring minimal oscillations, low energy consumption, and stability of UAVs and hanging loads. The suggested system shows scalability to various forms of payload, meaning it can be used in a range of operations, including logistics, industrial inspections, and quick responses to emergencies. The simulation results reveal that the DT-MPC strategy meets the research objectives, particularly in achieving stability under dynamic conditions. Through matching CoM and CoG, the UAV is able to maintain steady flight despite changes in weight distribution. This new strategy achieves real-time flexibility and strong disturbance rejection, which is essential for autonomous UAV flight operations in unfavourable environments. Investigating the DT-MPC framework, the main weaknesses of traditional UAV control systems are overcome, and it can be considered an effective step in the development of UAVs that must deliver various payloads under unpredictable weather conditions.

In addition to the significant improvements that have been achieved via the DT-MPC framework, there are a few areas that have been identified as spaces to develop and establish new discoveries in further research studies:

Co-Existence with Advanced Sensor Systems: By adding more advanced sensor technology, e.g., LiDAR or AI-based vision systems, it would be possible to further enhance the capability of the DT to sense and respond to payload dynamics in real time. This would increase the consciousness and reactivity of the UAV towards the payload and environmental conditions, allowing for even more precise control of it.

Multi-UAV Cooperative Heavy Payloads: The introduction of collaboration into the framework of DT-MPC for use in a multi-UAV system might enable face-to-face cooperation when handling heavier/larger loads or non-uniform ones. Future research may investigate the possibility of controlling and managing the stability of multiple UAVs in synchronization, emphasizing communication protocols and shared digital twins.

Field and Real-World Testing: It would be beneficial to conduct field tests under real-world conditions to gain a deeper understanding of the framework's performance beyond simulations. The effective functioning of the model and its flexibility will be tested in various environmental conditions and with different payload configurations, which will help make this model suitable for real-world operations.

Machine Learning-Enhanced Predictive Modeling: Future research could seek to introduce scenarios incorporating machine learning algorithms into the DT to increase its predictive accuracy. Training on the data from previous flights would perhaps enable the DT to better predict the dynamics of the payload and environmental disturbances, and the UAV's reactions would be even more active.

Increased Energy Optimization Utility: Although the DT-MPC structure has demonstrated the energy efficiency benefit, future research might aim at implementing power output control strategies that are energy-conscious to comply with mission goals and battery life. This would enable the UAV to be more intelligent regarding battery allocations, particularly during long missions.

Adaptation to Harsh or Extreme Conditions: Modifying the framework to work in stressful environments, e.g., high-altitude or windy conditions, would lead to new UAV uses. Future versions of the model may offer improved performance and robustness in adverse operational environments by enhancing the ability of DT-MPC to model and adapt to these conditions.

Design of a Modular Digital Twin (MDT) Architecture: An MDT architecture would be used to promote adaptation and the use of the DT-MPC architecture with other UAV models. Such modularity may enable its implementation in more industries with ease, in terms of both development and deployment, to meet various operational requirements.

Author Contributions: U.F.: Methodology, Conceptualization, and Writing—Original Draft, B.K.: Supervision and Conceptualization. S.M.A.: Investigation, Review and Editing of Draft, and Validation. Z.U.: Project Administration, Visualization, and Formal Analysis. All authors have read and agreed to the published version of the manuscript.

Funding: This research received no external funding.

Informed Consent Statement: Not applicable.

Data Availability Statement: The original contributions presented in this study are included in the article. Further inquiries can be directed to the corresponding author.

Conflicts of Interest: The authors declared no conflicts of interest.

Abbreviations and Nomenclature

The following abbreviations and nomenclatures are used in this manuscript:

Abbreviation	**Definition**
DT	Digital Twin
MPC	Model Predictive Control
UAV	Unmanned Aerial Vehicle
CoG	Center of Gravity
CoM	Center of Mass
EKF	Extended Kalman Filter
SMC	Sliding-Mode Controller
QP	Quadratic Programming
DoF	Degrees of Freedom
ARIMA	AutoRegressive Integrated Moving Average
IMU	Inertial Measurement Unit
GPS	Global Positioning System
FOV	Field of View
OTA	Over-the-Air
MTBF	Mean Time Between Failures
SIL	Safety Integrity Level
Nomenclature	
Symbol	**Definition**
$\mathbf{p}$	Position vector in inertial frame $\mathcal{I}$ ($\mathbb{R}^3$)
$\mathbf{v}$	Velocity vector in body-fixed frame $\mathcal{B}$ ($\mathbb{R}^3$)
$\boldsymbol{\omega}$	Angular velocity in body-fixed frame $\mathcal{B}$ ($\mathbb{R}^3$)
m	Mass of UAV (kg)
I	Inertia tensor of UAV ($\mathbb{R}^{3\times3}$)
R	Rotation matrix from body frame to inertial frame ($\mathbb{R}^{3\times3}$)
$\mathbf{g}$	Gravity vector, $[0, 0, -g]^T$, where $g = 9.81\,\mathrm{m/s^2}$

$\mathbf{f}_t$	Collective thrust vector, $[0, 0, T]^T$ ($T > 0$, N)
$\mathbf{f}_d$	Aerodynamic drag force on UAV
$\mathbf{f}_p$	Payload force acting on UAV
$\boldsymbol{\tau}_t$	Attitude torques from differential rotor speeds, $[\tau_x, \tau_y, \tau_z]^T$ (Nm)
$\boldsymbol{\tau}_p$	Payload torque acting on UAV
$\mathbf{x}$	State vector, $[\mathbf{p}^T, \mathbf{v}^T, \boldsymbol{\theta}^T, \boldsymbol{\omega}^T]^T$ ($\mathbb{R}^{12}$)
$\boldsymbol{\theta}$	Euler angle (rad)
$\mathbf{u}$	Control input vector, $[T, \tau_x, \tau_y, \tau_z]^T$ ($\mathbb{R}^4$)
A	System matrix, $\frac{\partial f}{\partial \mathbf{x}}\|_{\mathbf{x}_e}$
B	Input matrix, $\frac{\partial f}{\partial \mathbf{u}}\|_{\mathbf{u}_e}$
$\mathbf{z}$	State deviation, $\mathbf{x} - \mathbf{x}_e$
$\mathbf{w}$	Perturbation input
$m_p(t)$	Time-varying payload mass (kg)
$\mathbf{r}_p(t)$	Relative position vector from UAV CoM to payload CoM ($\mathbb{R}^3$)
$I_p(t)$	Payload inertia tensor ($\mathbb{R}^{3\times3}$)
$\mathbf{v}_p$	Payload-relative velocity, $\dot{\mathbf{r}}_p + \mathbf{v} + \boldsymbol{\omega} \times \mathbf{r}_p$
$\mathbf{f}_{a,p}$	Payload-specific aerodynamic drag force
$\boldsymbol{\omega}_p$	Payload angular rate, $\boldsymbol{\omega} + \dot{\boldsymbol{\theta}}_p$
$\boldsymbol{\theta}_p$	Payload Euler angle (rad)
$M(t)$	Total mass, $m + m_p(t)$ (kg)
$C(\cdot)$	Coriolis/centripetal matrix (skew-symmetric)
$C_r(\cdot)$	Rotational cross-terms matrix
$\Delta I(t)$	Parametric uncertainty in inertia tensor
$\hat{\mathbf{x}}$	Digital twin state estimate ($\mathbb{R}^{12}$)
$\mathbf{y}$	Sensor measurement vector
H	Measurement matrix
$\boldsymbol{\nu}$	Measurement noise, $\sim \mathcal{N}(0, \Sigma_\nu)$
K_k	Kalman filter gain at step k
$P_{k\|k-1}$	Predicted covariance matrix
Q	Process noise covariance matrix
Γ	Disturbance distribution matrix
Σ_w	Disturbance covariance matrix
$\hat{\mathbf{w}}$	Disturbance forecast via ARIMA model
$\boldsymbol{\eta}_i$	ARIMA noise, $\sim \mathcal{N}(0, \Sigma_\eta)$
Δt_k	Adaptive sampling time step (s)
J_k	MPC stage cost function
$\mathbf{x}_{ref}$	Reference state trajectory
Q, R, P_f	MPC weighting matrices for state error, control effort, and terminal cost
$\mathcal{W}$	Disturbance set, $\{\mathbf{w} : \|\mathbf{w}\| \leq \epsilon_w\}$
$\mathcal{E}$	Error set for tube MPC
$\mathcal{X}_f$	Robust invariant terminal set
$\boldsymbol{\xi}$	Augmented state vector, $[\mathbf{x}^T, \mathbf{r}_p^T, \boldsymbol{\theta}_p^T]^T$ ($\mathbb{R}^{18}$)
$\mathbf{d}(t)$	Disturbance vector, $[\Delta m_p(t), \Delta I_p(t), \Delta C_{d,p}(t)]^T$
$\mathcal{F}$	Nonlinear dynamics function
$\bar{A}, \bar{B}, \bar{G}$	Linearized system, input, and disturbance matrices
K_f	Filter gain for DT error dynamics
$\mathcal{D}$	Polytope of disturbances
V_f	Terminal cost function, $\mathbf{z}^T P_f \mathbf{z}$

Appendix A

Table A1. Comprehensive parameters for model evaluation.

Parameter	Value	Description
Simulation Time	10 s	Total time duration for simulation
Time Step	0.01 s	Discretization interval for simulation
Mass of UAV (m)	1.5 kg	Mass of UAV, including structural weight
Payload Mass	0.5 kg	Weight of payload carried by UAV
Max Thrust	15 N	Maximum thrust force UAV motors can exert
Max Control Torque	0.5 Nm	Maximum torque applied for attitude control
Air Density (ρ)	1.225 kg/m^3	Standard air density at sea level used for aerodynamic calculations
Drag Coefficient (C_d)	0.05	Aerodynamic drag coefficient of UAV
Gravity (g)	9.81 m/s^2	Acceleration due to gravity
Prediction Horizon (N)	10	Horizon length for MPC predictions
Control Horizon	5	Control horizon for MPC, determining number of steps over which control inputs are optimized
Sampling Rate	100 Hz	Frequency at which digital twin updates predictions and receives feedback
MPC Weight on Position	1.0	Weighting factor for position error in MPC cost function
MPC Weight on Velocity	0.5	Weighting factor for velocity adjustments in MPC cost function
MPC Weight on Control Effort	0.1	Weighting factor penalizing excessive control efforts in MPC optimization
Actuator Response Time	0.05 s	Delay in actuator response to control signals
Stability Zone Threshold	0.1 m	Distance threshold for acceptable stability deviations in CoM and CoG alignment
Accelerometer Noise	0.001 g/$\sqrt{\text{Hz}}$	Accelerometer noise density
Magnetometer Accuracy	±2°	Heading accuracy from magnetometer
Barometer Resolution	0.1 hPa	Pressure sensor resolution
Rotor Speed Limits	0–3000 RPM	Maximum and minimum rotor speeds for thrust generation
Rotor Inertia (I_r)	0.0001 kg·m^2	Moment of inertia for each rotor
Arm Length (L)	0.25 m	Distance from center to each motor
Number of Rotors	4	Quadcopter configuration
Propeller Diameter	0.254 m	Diameter of each propeller
Propeller Pitch	0.114 m	Pitch of propeller blades
Thrust Coefficient (C_T)	1.2×10^{-5}	Thrust coefficient for propeller
Torque Coefficient (C_Q)	1.4×10^{-7}	Torque coefficient for propeller
Roll Moment Arm	0.25 m	Distance affecting roll torque generation
Pitch Moment Arm	0.25 m	Distance affecting pitch torque generation
Yaw Moment Arm	0.12 m	Distance affecting yaw torque generation
Payload Attachment Stiffness (k_p)	1000 N/m	Spring constant for payload attachment modeling
Payload Damping Coefficient (c_p)	50 Ns/m	Damping factor for payload oscillations
Payload Shape Factor	0.5–2.0	Geometric factor for irregular payloads
Payload Density Variation	±20%	Variation in payload material density
Payload Surface Roughness	0.1–1.0 mm	Surface texture affecting aerodynamics
Payload Attachment Points	4	Number of attachment points to UAV
Attachment Point Stiffness	800 N/m	Individual attachment spring constant
Cable Length (If Applicable)	0.3 m	Length of suspension cables
Cable Stiffness	2000 N/m	Elastic modulus of suspension cables

Table A1. *Cont.*

Parameter	Value	Description
Payload Rotation DOF	2	Degrees of freedom for payload rotation
Payload Translation DOF	3	Degrees of freedom for payload translation
Wind Speed (v_w)	0–10 m/s	Variable wind speed in simulation
Wind Direction	Variable	Variable wind direction (0°-360°)
Turbulence Intensity	0.1–0.3	Normalized turbulence intensity factor
Ground Effect Height	0.5 m	Height threshold for ground effect modeling
Ground Effect Gain	0.3	Gain reduction due to ground effect
Turbulence Filter Bandwidth	10 Hz	Cutoff frequency for turbulence filtering
Wind Compensation Gain	0.7	Gain for wind disturbance rejection
Thermal Current Detection	±0.5 m/s	Vertical air current detection threshold
Solar Radiation Model	Variable	Environmental heat input model
Humidity Effects	0-100%	Relative humidity impact on performance
Battery Capacity	2200 mAh	Total energy available for UAV's flight operations
Battery Voltage	22.2 V	Nominal voltage for LiPo battery pack
Battery Discharge Rate (C)	30C	Maximum continuous discharge rate
Motor Efficiency	85%	Electrical to mechanical power conversion efficiency
Emergency Landing Threshold	10%	Battery threshold for emergency procedures
Maximum Flight Duration	15 min	Maximum continuous flight time
Sensor Update Rate	200 Hz	IMU sensor data frequency
GPS Update Rate	10 Hz	Global positioning system update frequency
Vision Sensor FOV	120°	Field of view for onboard camera
Vision Sensor Resolution	640 × 480	Pixel resolution of vision system
Vision Processing Latency	0.02 s	Delay in computer vision processing
Temperature Compensation	−20 °C to 60 °C	Operating temperature range for sensors
Obstacle Detection Range	10 m	Forward-looking sensor range
Communication Bandwidth	1 Mbps	Data link bandwidth for DT synchronization
Communication Latency	5 ms	Average communication delay
DT Synchronization Rate	100 Hz	Frequency of digital twin state synchronization
Control Loop Frequency	100 Hz	Main control algorithm execution rate
Computation Platform	NVIDIA Jetson	Embedded computing platform for control
Processor Clock Speed	2.2 GHz	CPU clock frequency
GPU CUDA Cores	256	Parallel processing cores for optimization
Memory Capacity	4 GB LPDDR4	RAM available for real-time computation
Storage Capacity	32 GB eMMC	Non-volatile storage for logging
Operating System	Ubuntu 18.04	Linux distribution for real-time operations
State Estimation Filter	EKF	Extended Kalman filter for state estimation
Kalman Gain Adaptation	Adaptive	Online adaptation of filter gains
QP Solver	OSQP	Quadratic programming solver used
QP Solver Tolerance	1×10^{-6}	Convergence tolerance for optimization
Disturbance Model	ARIMA (2,1,2)	Autoregressive model for disturbance prediction
Control Gain for Position	0.8	Proportional gain for position adjustments
Control Gain for Attitude	1.2	Proportional gain for attitude stabilization
Rate Limits	±50°/s	Maximum angular rates for attitude
Acceleration Limits	±5 m/s^2	Linear acceleration constraints
Jerk Limits	±10 m/s^3	Smoothness constraints on acceleration
Collision Avoidance Margin	2 m	Safety margin for obstacle avoidance
Fail-Safe Altitude	5 m	Minimum altitude for safe operations
Geofence Radius	500 m	Operational area boundary
Actuator Saturation Limits	±100%	Percentage limits on actuator commands
Waypoint Tolerance	0.5 m	Position accuracy for waypoint following

Table A1. *Cont.*

Parameter	Value	Description
Coupled Mode Frequencies	1–5 Hz	Natural frequencies of coupled modes
Damping Ratio	0.1–0.3	Damping ratio for coupled oscillations
Aerodynamic Damping	0.05–0.2	Aerodynamic contribution to damping
Control Allocation Matrix	4 × 4	Matrix mapping inputs to actuators
Trajectory Smoothing Factor	0.8	Factor for trajectory interpolation
Return-to-Home Speed	2 m/s	Speed for automated return procedures
Obstacle Avoidance Speed	1 m/s	Speed during obstacle avoidance maneuvers
Operating Temperature Range	0–40 °C	Environmental temperature limits
Dust/Debris Resistance	IP54	Ingress protection rating
Vibration Tolerance	5 g RMS	Vibration resistance specification
Shock Resistance	50 g	Impact resistance specification
MTBF	10,000 h	Mean time between failures
Safety Integrity Level	SIL 2	Functional safety classification
Software Update Mechanism	OTA	Over-the-air update capability
Diagnostic Logging	1 MB/flight	Flight data recording capacity
Health Monitoring	Real-time	Component health monitoring system
Cybersecurity Protocols	AES-256	Data encryption standards
EMI/EMC Compliance	FCC Part 15	Electromagnetic compatibility standards

References

1. Li, Y.; Liu, M.; Jiang, D. Application of unmanned aerial vehicles in logistics: A literature review. *Sustainability* **2022**, *14*, 14473. [CrossRef]
2. Saponi, M.; Borboni, A.; Adamini, R.; Faglia, R.; Amici, C. Embedded payload solutions in UAVs for medium and small package delivery. *Machines* **2022**, *10*, 737. [CrossRef]
3. Mishra, H.; Mishra, D.; Tiwari, A.K.; Nishad, D.C. Cost–Benefit Analysis of Sensing and Data Collection with Drones for IoT Applications. In *Machine Learning for Drone-Enabled IoT Networks: Opportunities, Developments, and Trends*; Springer Nature: Cham, Switzerland, 2025; pp. 141–168.
4. Pagare, P.N. Review of studies on the effects of various wind load parameters on tall buildings with irregular and diversified geometries. *J. Harbin Eng. Univ.* **2023**, *44*, 966–982.
5. Wanner, D.; Hashim, H.A.; Srivastava, S.; Steinhauer, A. UAV avionics safety, certification, accidents, redundancy, integrity, and reliability: A comprehensive review and future trends. *Drone Syst. Appl.* **2024**, *12*, 1–23. [CrossRef]
6. Takahashi, T.T.; Griffin, J.A.; Grandhi, R.V. High-Speed Aircraft Stability and Control Metrics. *Aerospace* **2024**, *12*, 12. [CrossRef]
7. Imran; Li, J. Drone Airflow Dynamics and Crop Interaction. In *UAV Aerodynamics and Crop Interaction: Revolutionizing Modern Agriculture with Drone*; Springer Nature: Singapore, 2025; pp. 91–130.
8. Mohsan, S.A.H.; Othman, N.Q.H.; Li, Y.; Alsharif, M.H.; Khan, M.A. Unmanned aerial vehicles (UAVs): Practical aspects, applications, open challenges, security issues, and future trends. *Intell. Serv. Robot.* **2023**, *16*, 109–137. [CrossRef] [PubMed]
9. Massaoudi, M.S.; Abu-Rub, H.; Ghrayeb, A. Navigating the landscape of deep reinforcement learning for power system stability control: A review. *IEEE Access* **2023**, *11*, 134298–134317. [CrossRef]
10. Rachakonda, A. Anti-Swing Control of Quadrotors During Human Interaction: An Adaptive Approach. Ph.D. Thesis, International Institute of Information Technology Hyderabad, Hyderabad, India, 2024.
11. Zaynab, S.; Kayode, S. Exploring the Role of IoT in Autonomous Logistics and Drone Delivery Systems. *SSRN* **2025**, 5157991. Available online: https://ssrn.com/abstract=5157991 (accessed on 28 April 2025).
12. Farid, U.; Khan, B.; Mehmood, C.A.; Ali, M.; Shi, Y. Coordinated Heterogeneous UAVs for Trajectory Tracking and Irregular Payload Transportation Using Sliding Mode Control. *Drones* **2025**, *9*, 314. [CrossRef]
13. Romeo, S.A.S.; Oz, F.; Kassem, A.K.; San, O.; Kara, K. Physics Informed Data Fusion Model for Uncertainty Quantification in Atmospheric Entry Vehicle Dynamic Stability. In Proceedings of the AIAA Aviation Forum and ASCEND 2024, Las Vegas, NV, USA, 29 July–2 August 2024; p. 4446.
14. Ahmad, M.; Zaheer, M.Z. Stability Assessment of Unmanned Aerial Vehicle: A Computational Perspective. *Int. J. Aeronaut. Space Sci.* **2025**, 1–28. [CrossRef]
15. Okasha, M.; Kralev, J.; Islam, M. Design and experimental comparison of pid, lqr and mpc stabilizing controllers for parrot mambo mini-drone. *Aerospace* **2022**, *9*, 298. [CrossRef]

16. Miloš, M.; Mirosavljević, P. Analysis of the Performance and Kinematics of the Movement of UAV. *FME Trans.* **2023**, *51*, 627–636. [CrossRef]
17. Hinss, M.F. Human-Drone Interaction: Taking into Account the Estimation of Operator Fatigue in the Design of Adaptive Interactions for the Control of Long-Endurance UAVs. Ph.D. Thesis, Institut Supérieur de l'Aéronautique et de l'Espace, Université de Toulouse, Toulouse, France, 2024.
18. Babu, C.S.; Pal, A. Enhancing Security for Unmanned Aircraft Systems in IoT Environments: Defense Mechanisms and Mitigation Strategies. In *Unmanned Aircraft Systems*; John Wiley & Sons, Inc.: Hoboken, NJ, USA, 2024; pp. 429–476.
19. Abro, G.E.M.; Abdallah, A.M. Digital twins and control theory: A critical review on revolutionizing quadrotor UAVs. *IEEE Access* **2024**, *12*, 43291–43307. [CrossRef]
20. Meng, W.; Zhang, X.; Zhou, L.; Guo, H.; Hu, X. Advances in UAV Path Planning: A Comprehensive Review of Methods, Challenges, and Future Directions. *Drones* **2025**, *9*, 376. [CrossRef]
21. McClellan, A.; Lorenzetti, J.; Pavone, M.; Farhat, C. A physics-based digital twin for model predictive control of autonomous unmanned aerial vehicle landing. *Philos. Trans. R. Soc. A* **2022**, *380*, 20210204. [CrossRef] [PubMed]
22. Saccani, D.; Cecchin, L.; Fagiano, L. Multitrajectory model predictive control for safe uav navigation in an unknown environment. *IEEE Trans. Control Syst. Technol.* **2022**, *31*, 1982–1997. [CrossRef]
23. Phadke, A.; Medrano, F.A. Towards resilient UAV swarms—A breakdown of resiliency requirements in UAV swarms. *Drones* **2022**, *6*, 340. [CrossRef]
24. Modi, H.; Su, H.; Liang, X.; Zheng, M. MorphoCopter: Design, Modeling, and Control of a New Transformable Quad-Bi Copter. *arXiv* **2025**, arXiv:2506.07204.
25. Ajakwe, S.O.; Kim, D. Facets of security and safety problems and paradigms for smart aerial mobility and intelligent logistics. *IET Intell. Transp. Syst.* **2024**, *18*, 2827–2855. [CrossRef]
26. Qian, C.; Liu, X.; Ripley, C.; Qian, M.; Liang, F.; Yu, W. Digital twin—Cyber replica of physical things: Architecture, applications and future research directions. *Future Internet* **2022**, *14*, 64. [CrossRef]
27. Nguyen, T.N.; Ponciroli, R.; Bruck, P.; Esselman, T.C.; Rigatti, J.A.; Vilim, R.B. A digital twin approach to system-level fault detection and diagnosis for improved equipment health monitoring. *Ann. Nucl. Energy* **2022**, *170*, 109002. [CrossRef]
28. Walton, R.B.; Ciarallo, F.W.; Champagne, L.E. A unified digital twin approach incorporating virtual, physical, and prescriptive analytical components to support adaptive real-time decision-making. *Comput. Ind. Eng.* **2024**, *193*, 110241. [CrossRef]
29. Emami, Y.; Li, K.; Almeida, L.; Zou, S.; Ni, W. On the use of immersive digital technologies for designing and operating UAVs. *arXiv* **2024**, arXiv:2407.16288. [CrossRef]
30. Souanef, T.; Al-Rubaye, S.; Tsourdos, A.; Ayo, S.; Panagiotakopoulos, D. Digital twin development for the airspace of the future. *Drones* **2023**, *7*, 484. [CrossRef]
31. Muhammad, A.Q. Digital Twin-Assisted Multi-Layer Network: Resource Optimization for Low-Latency and Energy-Efficiency. Ph.D. Thesis, Lakehead University, Thunder Bay, ON, Canada, 2024.
32. Nwamekwe, C.O.; Chikwendu, O.C. Machine learning-augmented digital twin systems for predictive maintenance in highspeed rail networks. *Int. J. Multidiscip. Res. Growth Eval.* **2025**, *6*, 1783–1795.
33. Arsalan, A.; Umer, T.; Rehman, R.A.; Abdelmoniem, A.M.; Mumtaz, S. Toward Collaborative Intelligence in Digital Twin-based Federated Deep Reinforcement Learning: Applications, Case Studies and Challenges. *IEEE Netw.* 2025, *early access*. [CrossRef]
34. Kim, W.; Kim, S.; Jeong, J.; Kim, H.; Lee, H.; Youn, B.D. Digital twin approach for on-load tap changers using data-driven dynamic model updating and optimization-based operating condition estimation. *Mech. Syst. Signal Process.* **2022**, *181*, 109471. [CrossRef]
35. Aliyari, M.; Wong, W.-K.; Bouteraa, Y.; Najafinia, S.; Fekih, A.; Mobayen, S. Design and implementation of a constrained model predictive control approach for unmanned aerial vehicles. *IEEE Access* **2022**, *10*, 91750–91762. [CrossRef]
36. Panjavarnam, K.; Ismail, Z.H.; Tang, C.H.H.; Sekiguchi, K.; Casas, G.G. Model Predictive Control for Autonomous UAV Landings: A Comprehensive Review of Strategies, Applications and Challenges. *J. Eng.* **2025**, *2025*, e70085. [CrossRef]
37. Geronel, R.S.; Botez, R.M.; Bueno, D.D. On the Effect of Flexibility on the Dynamics of a Suspended Payload Carried by a Quadrotor. *Designs* **2022**, *6*, 31. [CrossRef]
38. Peris, C.; Norton, M.; Khoo, S. Adaptive multi-surface sliding mode control with radial basis function neural networks and reinforcement learning for multirotor slung load systems. *Electronics* **2024**, *13*, 2424. [CrossRef]
39. Sadi, M.A.; Jamali, A.; Kamaruddin, A.M.N.A. Optimizing UAV performance in turbulent environments using cascaded model predictive control algorithm and Pixhawk hardware. *J. Braz. Soc. Mech. Sci. Eng.* **2025**, *47*, 396. [CrossRef]
40. Xu, T.; Liu, J.; Zhang, Z.; Chen, G.; Cui, D.; Li, H. Distributed MPC for trajectory tracking and formation control of multi-UAVs with leader-follower structure. *IEEE Access* **2023**, *11*, 128762–128773. [CrossRef]
41. Gräfe, A.; Trimpe, S. Event-triggered Robust Model Predictive Control under Hard Computation Resource Constraints. *arXiv* **2025**, arXiv:2504.19540. [CrossRef]
42. Prasad, G. Aerodynamics Principles and Advances in Unmanned Aerial Vehicles. In *Innovations and Developments in Unmanned Aerial Vehicles*; IGI Global Scientific Publishing: Hershey, PA, USA, 2025; pp. 129–144.

43. Hidayat, N.A.; Rosyid, D.M.; Hadiwidodo, Y.S. Sensitivity Study of Dynamic Response and Seismic Performance of Offshore Tripod Structure Under Variation of Center of Gravity Location. *Int. J. Mar. Eng. Innov. Res.* **2025**, *10*, 705–726.
44. Wang, F.; Nishter, Z. Real-time load forecasting and adaptive control in smart grids using a hybrid neuro-fuzzy approach. *Energies* **2024**, *17*, 2539. [CrossRef]
45. Mahdi, S.M.; Abdulkareem, A.I.; Humaidi, A.J.; Al Mhdawi, A.K.; Al-Raweshidy, H. Comprehensive Review of Control Techniques for Various Mechanisms of Parallel Robots. *IEEE Access* **2025**, *13*, 63381–63416. [CrossRef]
46. Xiao, J.; Zhang, R.; Zhang, Y.; Feroskhan, M. Vision-based learning for drones: A survey. *IEEE Trans. Neural Networks Learn. Syst.* **2025**, *36*, 15601–15621. [CrossRef]
47. Ozkat, E.C. Vibration data-driven anomaly detection in UAVs: A deep learning approach. *Eng. Sci. Technol. Int. J.* **2024**, *54*, 101702. [CrossRef]
48. Kidambi, K.B.; Tiwari, M.; Jayaprakash, A.K.; MacKunis, W.; Golubev, V. A sliding mode observer-based limit cycle oscillation suppression using a robust active flow control technique. In Proceedings of the 2022 IEEE Conference on Control Technology and Applications (CCTA), Trieste, Italy, 23–25 August 2022; pp. 516–521.
49. Alzorgan, H.; Razi, A.; Moshayedi, A.J. Actuator trajectory planning for uavs with overhead manipulator using reinforcement learning. In Proceedings of the 2023 IEEE 34th Annual International Symposium on Personal, Indoor and Mobile Radio Communications (PIMRC), Toronto, ON, Canada, 5–8 September 2023; pp. 1–6.
50. Moshayedi, A.J.; Roy, A.S.; Taravet, A.; Liao, L.; Wu, J.; Gheisari, M. A secure traffic police remote sensing approach via a deep learning-based low-altitude vehicle speed detector through uavs in smart cites: Algorithm, implementation and evaluation. *Future Transp.* **2023**, *3*, 189–209. [CrossRef]
51. Farid, U.; Khan, B.; Mehmood, C.A.; Ali, S.M.; Mehmood, F.; Ullah, Z. Autonomous Payload Delivery: A Sequential Approach Using Single and Heterogeneous Drones. *J. Eng.* **2025**, *2025*, 7618520. [CrossRef]

Disclaimer/Publisher's Note: The statements, opinions and data contained in all publications are solely those of the individual author(s) and contributor(s) and not of MDPI and/or the editor(s). MDPI and/or the editor(s) disclaim responsibility for any injury to people or property resulting from any ideas, methods, instructions or products referred to in the content.